nature communications

Article

https://doi.org/10.1038/s41467-026-68514-0

Bionic Janus hydrogel drives infected Achilles tendon regeneration via mechano-immune spatiotemporal steering

Received: 10 June 2025

Accepted: 5 January 2026

Published online: 20 January 2026

Check for updates

Jie Li[1,2,6], Zishuo Wang[3,6], Wenjing Yang[3,6], Yuchen Zhang[2], Yanjun Wang[4], Xuhui Wang[4], Hongrui Wang[4], Yang Xie[4], Shuogui Xu[4], Yan Shang[5], Chunyu Xue[1] ✉, Yuntong Zhang[3,4] ✉ & Shuo Fang[1,3] ✉

The healing of infected tendons is hindered by mechanical dysfunction, tissue adhesion, bacterial colonization, and immune imbalance. Inspired by the biphasic "adhesion-lubrication" structure of tendon sheaths, we developed a Janus hydrogel, named HAPP@H-EXO, for spatiotemporal repair. The material exhibits antifatigue properties and redistributes mechanical stress through a dynamic network formed by norbornylated PVA and boronic acid-modified hyaluronic acid-PVA. Its high-adhesion side integrates tissue via borate and hydrogen bonds, whereas the lotus leaf-induced low-adhesion side prevents postsurgical adhesion. The incorporation of oligo-polyethyleneimine and phenylboronic acid groups traps and kills bacteria, overcoming resistance. The pH-responsive release of hypoxic tendon stem cell exosomes reprogrammes macrophages via inhibition of the NF-κB pathway, reducing inflammation and promoting regeneration. In an infected Achilles tendon model, HAPP@H-EXO eliminated MRSA, suppressed early inflammation, and enhanced regeneration. Within 8 weeks, it significantly improved biomechanical strength, prevented adhesion, and restored motor function, establishing a mechan-oimmunotherapeutic strategy for infected tissue regeneration.

Tendons are dense fibrous connective tissues that connect muscle to bone[1]. Although ruptured tendons can typically be surgically restored to continuity and basic motor function owing to advances in technology, rerupture still occurs in approximately 5% of patients[2,3]. Although the intertendinous matrix in the Achilles tendon, which is the strongest and largest tendon in the human body, is characterized by fatigue resistance and low stiffness, Achilles rupture is among the most common types of tendon rupture, accounting for approximately 20.40% of tendon injuries[1,4]. There is a bimodal age distribution for tendon ruptures, with young adults between 25 and 40 years of age being more prone to injuries associated with high-energy activities, such as sports, and older adults approximately 60 years of age being more prone to spontaneous rupture of the degenerative Achilles tendon or chronic Achilles tendon rupture disease, both of which are characterized by insufficient mechanical strength of the tissues and reduced regenerative capacity, respectively, ultimately leading to poor healing and even rerupture[5].

Moreover, open wounds and surgical procedures can lead to bacterial infections in tendon tissue, and the effects can be devastating. First, the anatomical characteristics of the tendon, such as a dense extracellular matrix, inadequate blood supply, and thin soft-tissue coverage, make it one of the least resistant tissues to infection, and

[1]Department of Plastic Surgery, The First Affiliated Hospital of Naval Medical University, Shanghai, P. R. China. [2]Department of General Practice Residency Training Base, The First Affiliated Hospital of Naval Medical University, Shanghai, P. R. China. [3]School of Exercise and Health, Shanghai University of Sport, Shanghai, P. R. China. [4]Department of Orthopedic Surgery, The First Affiliated Hospital of Naval Medical University, Shanghai, P. R. China. [5]Department of General Practice, The First Affiliated Hospital of Naval Medical University, Shanghai, P. R. China. [6]These authors contributed equally: Jie Li, Zishuo Wang, Wenjing Yang. ✉e-mail: xcyfun@sina.com; Yuntong_zhang@smmu.edu.cn; fangshuo826@126.com

conventional drug treatment strategies are often unable to achieve adequate drug delivery to the entire infected area. Second, bacterial infection further aggravates the local inflammatory response, resulting in a vicious cycle of persistent and intense proinflammatory factor production, reactive oxygen species (ROS) overload and inhibition of anti-inflammatory signals, making it difficult for the microenvironment of the injured area to transition to a state conducive to tissue repair and regeneration and leading to the adhesion of peripheral inflammatory tissues, dysfunction of internal cellular functions, and severe dysregulation of exogenous and endogenous repair processes. Therefore, the repair of ruptured tendons with bacterial infection is a major and long-standing challenge in orthopaedic and sports medicine[2,6–8]. Globally, up to 17.05% of patients who undergo tendon repair surgery require secondary surgery or even experience functional impairment as a result of infection[9]. In recent years, biomaterials with mechanical adaptations, immunomodulatory functions, or antimicrobial properties have provided ideas to solve this problem; however, the existing systems remain insufficient in terms of biomimetic structure design, dynamic antimicrobial mechanisms, and inflammatory microenvironment regulation[10].

Regarding antimicrobial strategies, traditional drug therapy involving antibiotics has limited efficacy as a result of bacterial resistance, which has led to the widespread prevalence of multidrug-resistant bacteria such as MRSA[11]. In recent years, antimicrobial materials have started to be designed to actively capture and kill bacteria rather than have passive bactericidal effects[12]. Owing to its reversible diol-bonding property, the phenylboronic acid moiety has shown unique advantages in bacterial-specific recognition and capture[13]. The positive charge of cationic polymers (e.g., PEI) can physically disrupt bacterial cell membranes to achieve bactericidal effects and can effectively prevent drug resistance[14]. However, most existing studies focus on a single antimicrobial mechanism, and long-term studies on the evolution of bacterial resistance and other complex biological behaviours are lacking[13,15]. Therefore, the construction of antimicrobial systems with the ability to promote tendon repair in a spatiotemporal manner to achieve local drug delivery, exert robust bactericidal effects and prevent bacterial drug resistance is a core challenge in the design of biomaterials for the repair of ruptured tendon tissue infected with bacteria.

From a tissue engineering perspective, the mechanical protection and regulation of the regenerative microenvironment of natural tendons strongly depend on the precise biphasic structure of the tendon sheath[16,17]. The synovial sheath can achieve mechanical coupling with the tendon and avoid ectopic adhesion with surrounding tissues through the synergistic effect of "adhesion–lubrication." This dynamic equilibrium mechanism provides important insights for the design of biomimetic materials[18]. Although traditional hydrogel materials can mimic the properties of the extracellular matrix, they face limitations in terms of fatigue resistance and mechanical force redistribution in complex mechanical environments[19]. Recently, dynamic covalent bonding has been introduced to improve the mechanical responsiveness of materials, but a single network structure can hardly satisfy the conflicting demands of supporting strong tendon tissue adhesion and proper tendon gliding while preventing peripheral adhesion[20,21]. Therefore, the development of multifunctional hydrogels with a biomimetic Janus structure to achieve spatiotemporal reprogramming and restore mechanical function is key to overcoming the limitations of the currently employed technology.

Inflammatory microenvironment regulation is another key strategy to suppress exacerbated inflammatory responses and accelerate the process of tissue repair. Multiple adverse events, including ROS accumulation, mitochondrial dysfunction, and M1 macrophage polarization, trigger persistent inflammation, induce the formation of adhesions in surrounding tissues, and inhibit regeneration. Ultimately, these alterations significantly weaken the biomechanical function of the repaired tendon and increase the risk of rerupture[8,18,22,23]. Stem cell-derived exosomes can regulate inflammation at an early stage and promote regeneration at a later stage during the repair process of various tissues, such as the skin, bone, and myocardium[24–27]. In particular, hypoxic preconditioning significantly increases the load of various anti-inflammatory substances and improves hypoxia tolerance in the early stage of repair[28–30]. A population of regenerative tendon stem cells (TDSCs) located in a unique ecological niche of the tendon has been found to be critical for the functional regeneration of tendon tissue[31]. Therefore, the culture of TDSC-derived exosomes under hypoxic conditions may have unique applications in tendon injury repair, which is worth exploring. In addition, conventional delivery systems are not favourable for the long-term accumulation of exosomes in the local environment, and the drug release kinetics of these systems do not promote the repair process[32]. Biomedical hydrogels are structurally similar to natural extracellular matrix, and their good water retention ability and excellent cell biocompatibility make them ideal slow-release carriers for exosomes[33,34]. On this basis, the controlled release of exosomes by stimulus-responsive hydrogels can be achieved through intelligent design to simultaneously suppress inflammation and promote regeneration. In this study, the optimal utilization strategy of stem cell-derived exosomes in tendon repair was explored.

On the basis of the design concept of "structural biomimicry–functional coupling," we constructed a Janus hydrogel with spatiotemporal programming ability. The system simulates the biphasic mechanical properties of natural tendon sheaths through the synergistic effects of the PVA–NB covalent network and the HP–PVA dynamic network. In addition, the introduced PEI and phenylboronic acid moieties enable the trapping and killing of microbes, and the integrated Hypo-TDSC-Exos exert immunomodulatory effects. First, a dual hydrogel network with a high-strength covalent network backbone was developed to mimic the antifatigue and stress dispersion properties of the tendon matrix. Second, lotus leaf induction endowed the hydrogel with asymmetric adhesion properties, enabling strong adhesion and excellent bioactivity on the adjacent medial side of the Achilles tendon to provide mechanical support and a favourable microenvironment for tendon repair. Moreover, the outer layer was nonadhesive to the surrounding tissues, which reduced friction and cellular adhesion and thus prevented fibrotic scar formation. A phenylboronic acid group and PEI were added to capture the bacteria and physically disrupt their cell membranes to achieve efficient antibacterial and antibiofilm effects and prevent bacterial resistance. Additionally, a pH-responsive controlled-release system loaded with Hypo-TDSC-Exos was established to achieve temporal synergy between macrophage polarization regulation and tendon regeneration. Experiments in a model of Achilles tendon rupture combined with MRSA infection confirmed that HAPP@H-EXO could kill drug-resistant bacteria, prevent oxidative stress, inhibit inflammation, promote microangiogenesis and tendon cell differentiation and maturation, prevent adhesions in surrounding tissues, restore biomechanical strength, and improve behavioural function (Fig. 1).

Results

Preparation and characterization of the hydrogels

In this study, a high-strength hydrogel with a dual-cross-linking topology was developed by combining mercaptoalkene click chemistry with dynamic borate cross-linking. First, the amino group of 3-aminobenzeneboronic acid (PBA) was coupled with the carboxyl group of hyaluronic acid (HA) using an amide-bonding reaction in an EDC-HCl/NHS-catalysed system, and 3-aminobenzeneboronic acid-modified hyaluronic acid (HP) was successfully produced (Supplementary Fig. 1A). UV–Vis spectroscopy of HP revealed a characteristic absorption peak at 240 nm, which was consistent with the absorption properties of PBA endowed by its benzene ring structure

https://doi.org/10.1038/s41467-026-68514-0

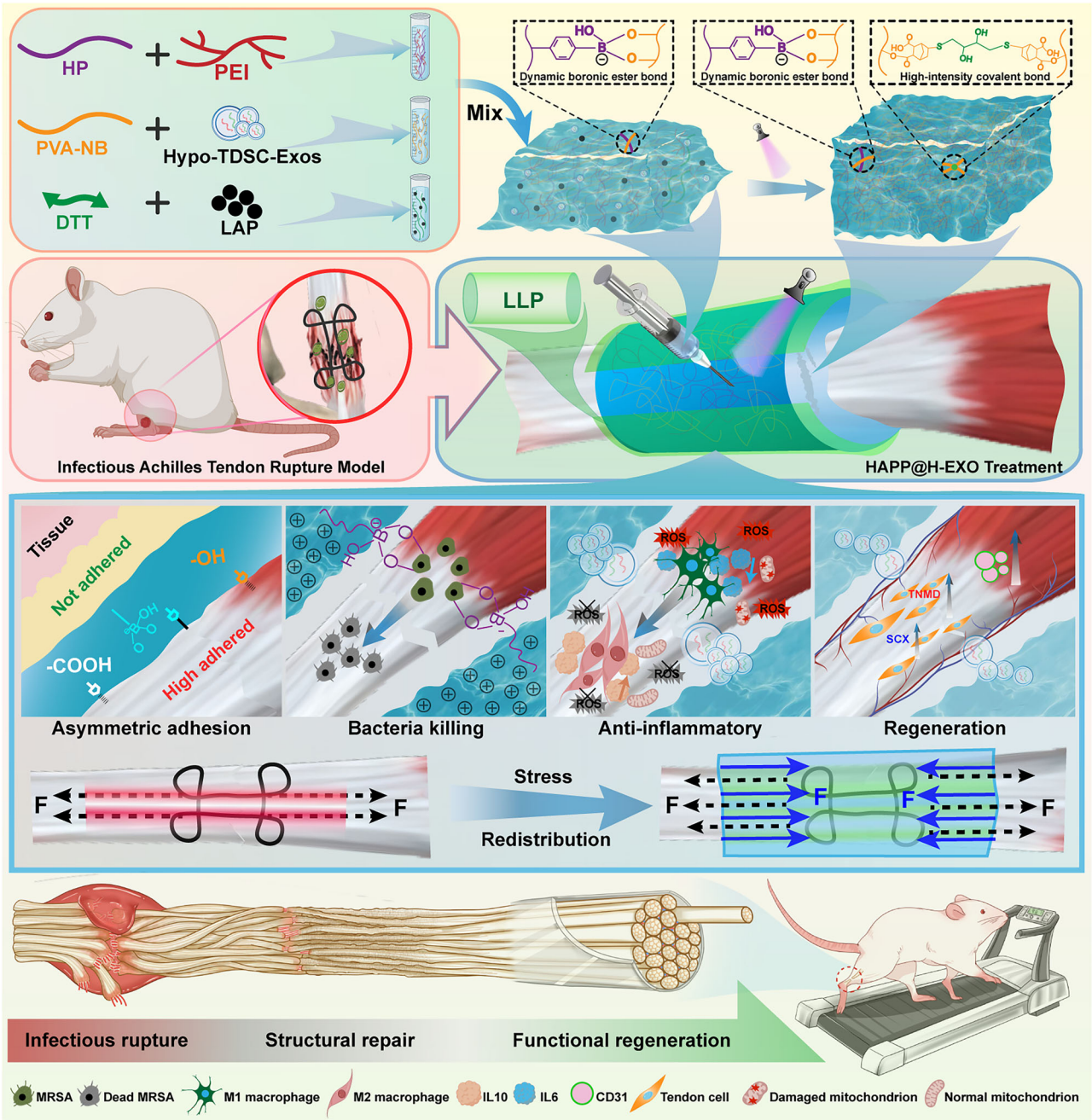

Fig. 1 | Schematic illustration of the design and mechanism. The bionic Janus hydrogel (HAPP@H-EXO) for the spatiotemporal repair of ruptured infected tendens.

(Supplementary Fig. 1B–D). By quantitatively analysing the intensity of the characteristic absorption peak of the PBA π-π* jump, the amount of PBA grafted on the HA molecular chain was determined to be 7.66 wt%. Additionally, norbornene anhydride was introduced into the main chain of PVA by esterification (Supplementary Fig. 2A), which introduced a double bond structure into the PVA molecular chain and created conditions for the subsequent cross-linking reaction. The 1H nuclear magnetic resonance (NMR) data (Supplementary Fig. 2B) revealed new characteristic peaks at 6.2 ppm (s, 2H, –CH=CH–), 3.3 ppm (s, 2H, –C=C–CH–), 3.1 ppm (s, 2H, –C=C–CH–CH–), and 1.3 ppm (s, 2H, $-CH_2-$). The degree of substitution of norbornene anhydride was determined to be 25.50 wt% by quantitative analysis of the integral values of the characteristic signal peaks. According to the calculation of the degree of substitution, the PVA-NB used in this work provided approximately 429 cross-linking reaction sites per chain. The above characterization results not only confirmed the successful preparation of HPs and PVA-NB but also revealed the extent of their modifications. Finally, the synthesized HP was mixed with PEI to form a mixture, which was subsequently mixed with a PVA-NB solution, and lithium phenyl (2,4,6-trimethylbenzoyl) phosphate (LAP) and dithiothreitol (DTT) were added to form a hydrogel precursor. The hydrogel precursor was irradiated with UV light to produce HAPP hydrogels. Hydrogels HAP, HAPP1, HAPP2, HAPP3, and HAPP4 were synthesized with different solid contents of PEI (0.00%, 1.10%, 1.70%, 2.30%, and 2.90%, respectively).

Basic characterization and mechanical properties of the hydrogels

The gelation performance of the HAPP hydrogels was evaluated by vial inversion (Fig. 2A), in which the HP solution was mixed with the PVA-

https://doi.org/10.1038/s41467-026-68514-0

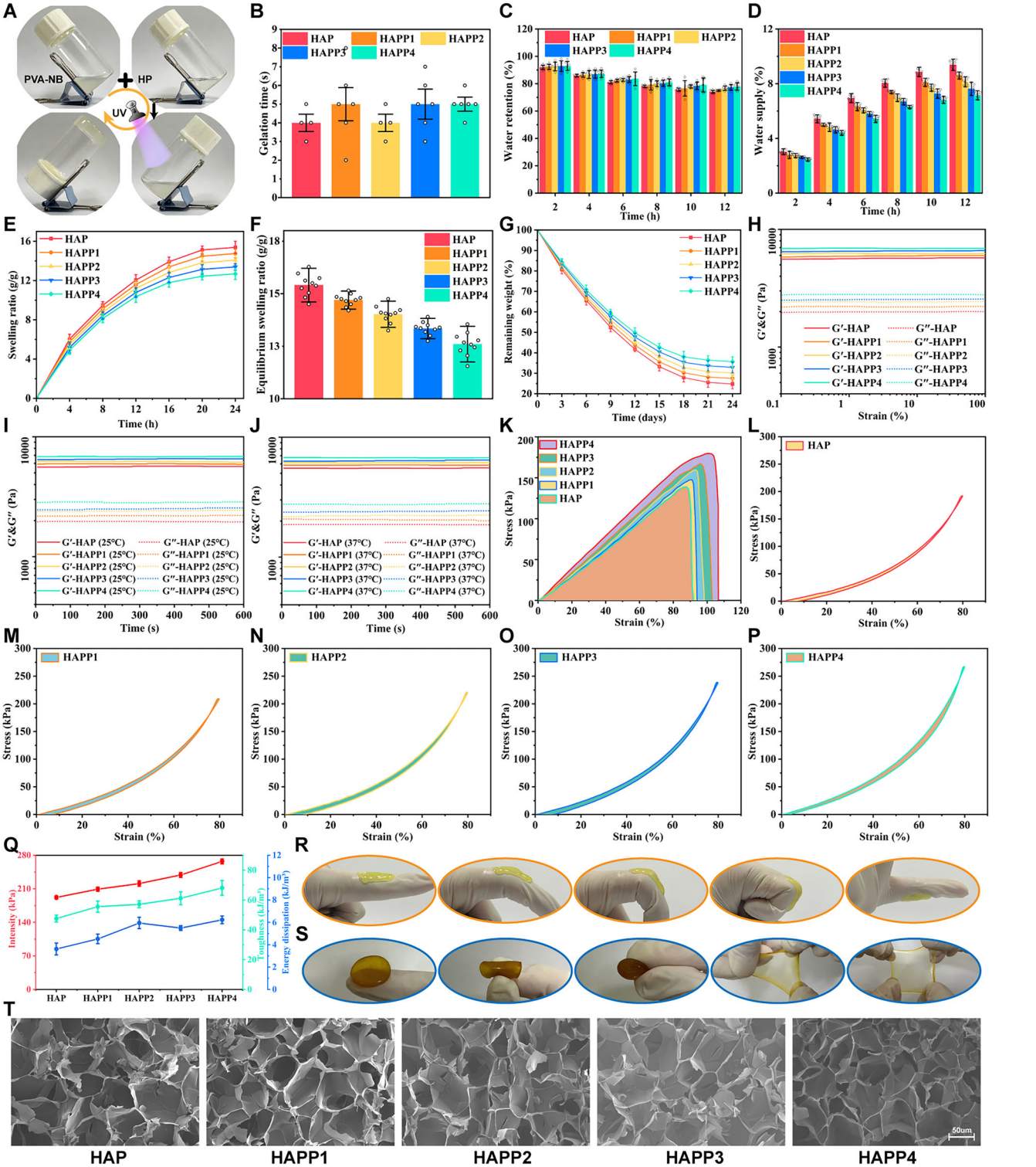

Fig. 2 | Basic characterization and mechanical properties of the hydrogels. **A** Gel formation process. **B** Gluing time ($n = 8$). **C** Water retention performance ($n = 7$). **D** Water supply performance ($n = 8$). **E** Swelling rate ($n = 10$). **F** Equilibrium swelling rate ($n = 10$). **G** Degradation curve ($n = 8$). **H** Rheological test. **I**, **J** Time scan test. **K** Tensile test curve. **L**–**P** Compression–unloading test. **Q** Strength, toughness, and energy dissipation ($n = 5$). **R** Macroscopic joint adhesion. **S** Macroscopic mechanical properties. **T** SEM image (n values derived from different experimental units. The data are presented as the mean ± standard deviation).

NB solution and cured into a gel by UV irradiation to achieve sulfhydryl-alkene click chemical gelation. Subsequent in situ gelation experiments (Fig. 2B) revealed that the gelation time of the hydrogels was within 7 s, confirming their excellent in situ gelation performance and laying a foundation for the subsequent design of Janus hydrogels mimicking the tendon sheath. Water retention and water supply performance tests (Fig. 2C, D) revealed that the water retention rate of the hydrogels was greater than 74.07 ± 1.23% after 12 h at 37 °C, and the water supply rate reached 7.21 ± 0.38%, which is favourable for tendon repair. Swelling analysis revealed that the equilibrium swelling rate of

all the hydrogels was greater than 12.68 ± 0.57 g/g in a pH 7.4 solution (Fig. 2E, F). The equilibrium swelling rate of the HAPP-treated hydrogels decreased with increasing PEI content, which was related to the increased density of the three-dimensional hydrogel structure. The moderate swelling property of the hydrogels not only endows them with structural integrity but also enables the absorption of exudate from the damaged tissue site[35]. In addition, in vitro degradation experiments (Fig. 2G) revealed that all the hydrogels degraded to less than 49.81 ± 2.42% on day 12 in a PBS solution at pH = 7.4, and their degradation cycle extended to more than 24 days, which provided a carrier for the long-lasting controlled release of nanoparticles throughout the tendon repair cycle. Scanning electron microscopy (SEM) results (Fig. 2T) revealed that all the groups of hydrogels presented uniform and interconnected three-dimensional topological network structures, in which the average pore size of HAP was 71.50 ± 3.34 μm, whereas that of HAPP4 decreased to 65.41 ± 3.09 μm (Supplementary Fig. 3A), which was essentially due to the increase in the cross-linking density of the three-dimensional network caused by the increased PEI content.

Rheological tests revealed that the storage modulus (G′) values of the hydrogels were always greater than the loss modulus (G″) values and that the G′ and G″ values did not significantly change as the strain increased from 0.1% to 100% (Fig. 2H). These findings indicated that the hydrogels had a wide linear viscoelastic zone and could withstand large strains. Time-scan tests (Fig. 2I, J) revealed that the G′ and G″ values of the hydrogels did not change significantly within 600 s at 25 °C and 37 °C and that the G′ values were greater than the G″ values, indicating that the topological network structure of the hydrogels was well stabilized, which strongly supported their ability to protect mechanical function and repair tendons. The tensile test results (Fig. 2K, Supplementary Fig. 3B) revealed that the strengths of the hydrogels were 138.94 ± 3.61 kPa (HAP), 147.62 ± 5.67 kPa (HAPP1), 159.61 ± 6.54 kPa (HAPP2), 167.05 ± 7.39 kPa (HAPP3), and 179.81 ± 7.21 kPa (HAPP4). The toughness values were 60.21 ± 2.54 kJ/m^3 (HAP), 66.39 ± 4.35 kJ/m^3 (HAPP1), 74.01 ± 4.21 kJ/m^3 (HAPP2), 83.11 ± 6.8 kJ/m^3 (HAPP3), and 99.41 ± 7.30 kJ/m^3 (HAPP4). This result revealed the good mechanical fitness of the tendon, which was closely related to the dynamic cross-linking of its internal PVA-NB high-strength covalent backbone and borate ester bonding. The incremental increases in these values among the hydrogels might be attributed to the increased amount of PEI in the system, which might have formed more cross-linking sites with the PVA-NB and HP molecular chains through hydrogen bonding. Compression loading–unloading tests (Fig. 2L–P) revealed that all the groups of hydrogels had small hysteresis loops, indicating that the hydrogels dissipated less energy after 80% compression. Further statistical analysis (Fig. 2Q) revealed that the strength of all the hydrogels was greater than 192.11 ± 3.23 kPa, the toughness was greater than 47.56 ± 2.35 kJ/m^3, and the strength and toughness of HAPP4 reached 267.20 ± 4.96 kPa and 68.09 ± 4.93 kJ/m^3, respectively. Notably, the energy dissipation of the hydrogels was as low as 6.22 ± 0.34 kJ/m^3 or lower. These findings suggested that hydrogels were able to prevent fatigue damage to materials by reducing internal network fracture through a more uniform stress distribution under the high-intensity dynamic loading of tendon gliding[36]. As shown in the physical drawings (Fig. 2R, S), the hydrogel could be tightly adhered to the finger joints without being affected by joint movement, and there was no breakage after folding and multisurface stretching. These findings confirmed that the hydrogel not only had excellent adhesion properties but also good mechanical properties, which was consistent with the compression test results.

In conclusion, with an appropriate number of degradation cycles, the HAPP hydrogels provided continuous mechanical support during the inflammatory phase (0–1 week) and proliferative phase (1–6 weeks) of tendon healing. Moreover, they release exosomes via gradient degradation, synergistically exerting anti-inflammatory, pro-angiogenic, and pro-cell migration effects[37]. Their structural design can adapt to the high-intensity dynamic loads of tendon gliding, significantly enhancing mechanical stability and stress buffering performance[20,38]. This dual optimization of temporal matching and mechanical adaptation ensures that the HAPP hydrogels provide suitable microenvironmental support throughout the entire healing process.

Hydrogels have increased fatigue resistance and can redistribute mechanical stress

The mechanical suitability of HAPP hydrogels for postoperative tendon repair was further investigated. The results of 100 cycles of compression loading–unloading tests (Fig. 3A, Supplementary Fig. 4A) revealed that the hysteresis lines of each hydrogel group almost overlapped and that the stress reduction rate was negligible, confirming the excellent fatigue resistance of the HAPP hydrogel. The compressive stress–time curves (Fig. 3B, Supplementary Fig. 4B) revealed that the stresses of the HAPP hydrogels did not decrease significantly with an increasing number of cycles, and the stresses of HAPP3 and HAPP4 were still as high as 243.21 kPa and 261.50 kPa, respectively, after 100 cycles. The above data indicated that the hydrogels had excellent antifatigue properties and could prevent further tears under dynamic stress, thus providing long-term stable mechanical support for tendons after surgery. Static tensile tests and static compression tests (Fig. 3C, D, Supplementary Fig. 4C, D) revealed that the resilience of the hydrogels did not decrease significantly after they reached a specific strain value, which suggested that the HAPP hydrogels experienced little energy dissipation. This phenomenon was attributed to the fact that the topological network of the HAPP hydrogels is mainly a rigid network structure mediated by covalent bonds, which can effectively inhibit the stress relaxation and creep of the hydrogels, thus contributing to the continued excellent elastic recoil behaviour of the hydrogels. The stress dispersion mechanism of the HAPP hydrogel is shown in Fig. 3E. Under the dynamic loading of a tendon, the hydrogel strongly adhered to the surface of the tendon and dispersed the stress rapidly through the topological network interlocked with the tissue interface, which resulted in a homogeneous distribution of the stress in the hydrogel and thus effectively avoided the concentration of stress at the tendon suture[39]. Moreover, the rigid topological network constructed by covalent bonds absorbed energy through elastic deformation and converted it into elastic potential energy. Combined with the low energy dissipation of the hydrogel matrix, the topological network continued to exhibit resilient energy. This process enabled the hydrogel to avoid secondary tendon rupture through dynamic load cushioning[38].

To further quantitatively evaluate the advantages of HAPP3 in terms of interfacial stress dispersion and transfer during tendon repair, we employed three-dimensional finite element analysis simulations. The results revealed that HAPP3 could effectively disperse the stress concentration at the suture site while synchronously transferring the load uniformly to the entire edge of the tendon (Supplementary Fig. 15A). As shown in Supplementary Fig. 15B, during the 3-second loading phase (with a load of 0.1 N), the stress statistics of 10 grid points at the tendon edge indicated that HAPP3 increased the stress in this region to approximately 16.38 kPa, which was significantly greater than that of the untreated group (<4 kPa). In the subsequent 5-second static maintenance phase, while the suture stress continued to decrease, the stress fluctuation at the tendon edge was only 5.33 Pa, demonstrating excellent stress redispersion capability and stress transfer stability. The stress distribution heatmap further confirmed that HAPP3 formed a continuous high-stress zone at the edge of the tendon, resulting in the redispersion and transfer of loads among the suture, interface, and tendon and effectively reducing the risk of stress concentration. Moreover, by promoting the contact of broken ends to optimize matrix remodelling and healing, HAPP3 provided an innovative material solution combining mechanical adaptability and bioactivity for postoperative repair[35].

https://doi.org/10.1038/s41467-026-68514-0

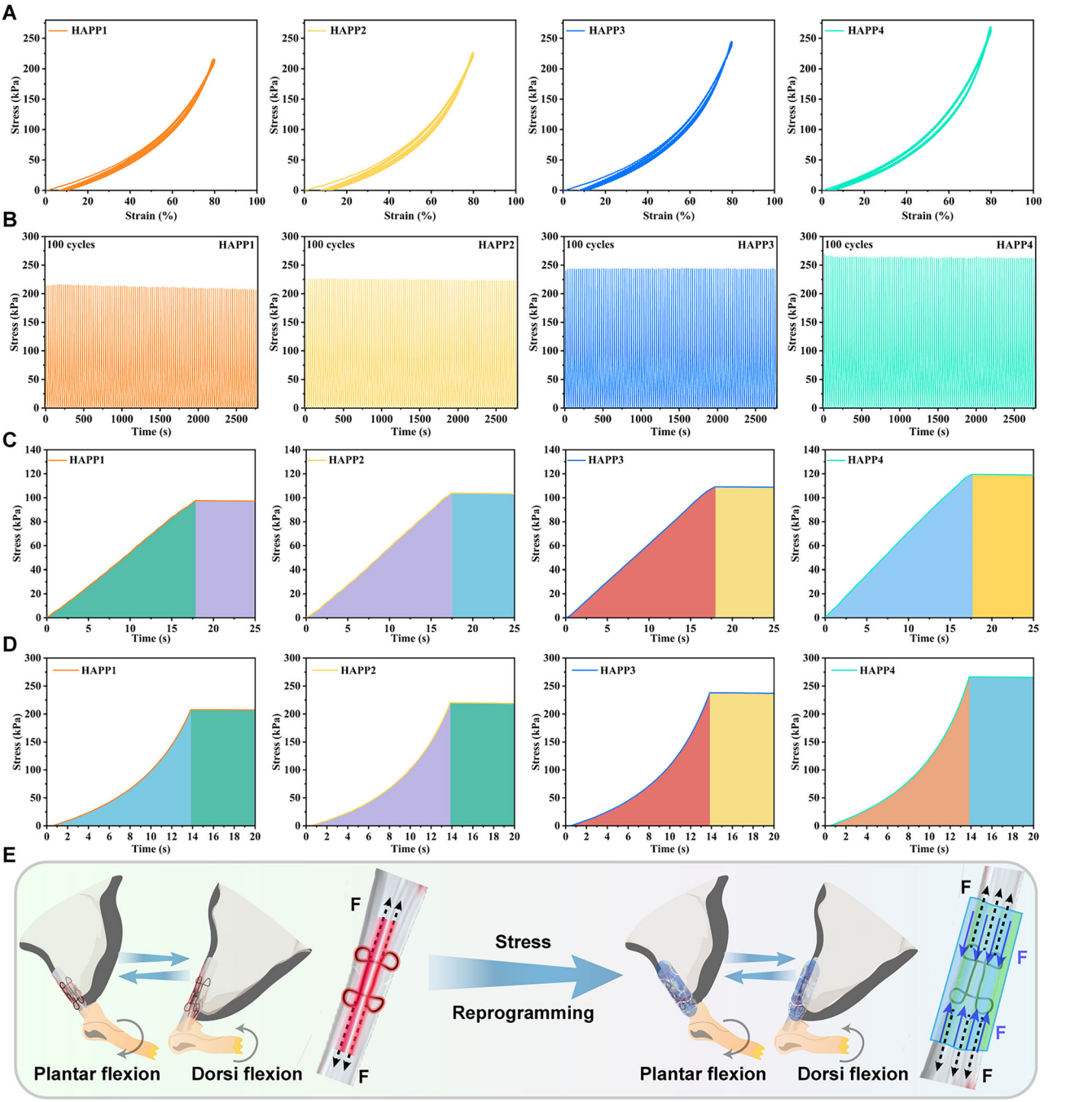

Fig. 3 | The hydrogel enables fatigue resistance and stress redistribution. A The 100 compression loading–unloading tests ($n = 4$). **B** Time–stress curves for the 100 compression load–unload tests ($n = 4$). **C** Time–stress curve of the static compression test ($n = 4$). **D** Time–stress curve of the static tensile test ($n = 4$). **E** Stress dispersion diagram (n values derived from different experimental units).

In conclusion, because the rigid topological network is mediated by high-strength covalent bonds, HAPP hydrogels achieved energy conversion and mechanical stress redistribution with excellent fatigue resistance and resilience. These findings demonstrated that hydrogels were highly compatible with the mechanical properties of natural tendons.

Self-healing, injectable, adaptive and wet adhesion properties of the hydrogels

As shown in Supplementary Fig. 5A, the two HAPP3 hydrogels were cut into two pieces and fused with each other after 24 h, and their integrity was maintained under the conditions of lifting and pulling from both sides. Tensile tests were performed on the fused hydrogels. The results (Supplementary Fig. 5B–F) revealed that the fracture load of each group of fused hydrogels linearly increased. The self-healing efficiency of all the groups of hydrogels reached more than 40.98 ± 2.15%, indicating that all the groups of hydrogels possessed excellent self-healing properties, which was attributed mainly to the dynamic borate and hydrogen bonding forces in the system at the interfaces (Supplementary Fig. 5G, H)[40,41]. The hydrogel precursor was injected into holes made in pig livers using a syringe, and the gel was formed in situ under UV light. It was found (Supplementary Fig. 5I) that the HAPP3 hydrogel could be extruded uniformly through the holes and expanded slowly until it filled the holes. The pig liver was subsequently flushed and

folded, and the hydrogel still adhered to the defects, confirming its excellent injectability, self-adaptability, and wet adhesion ability.

Lap-shear tests were performed on pigskin soaked in PBS for 1 h (Supplementary Fig. 6A). The results (Supplementary Fig. 6B, C) revealed that the adhesion forces of the hydrogels in all the groups were greater than 27.63 ± 0.83 kPa and even reached 33.75 ± 0.74 kPa and 34.85 ± 0.98 kPa for HAPP3 and HAPP4, respectively. A real-time monitoring system was used to test the ability of the hydrogels to seal the holes created in the small intestine and pig skin, and the maximum burst pressure represented the adhesion capacity of the hydrogels (Supplementary Fig. 6D). In the holes of the pigskin, the hydrogels could withstand a burst pressure of 221.12 ± 5.33 mmHg or more (Supplementary Fig. 6E). In the small intestine, the hydrogels could withstand a burst pressure of 198.47 ± 5.08 mmHg or more (Supplementary Fig. 6F). The above experimental results confirmed the excellent wet adhesion properties of the HAPP hydrogels, which were attributed mainly to the dynamic borate and hydrogen bonding forces established at the hydrogel–tissue interface (Supplementary Fig. 6J)[42]. This feature facilitated stable adhesion of the hydrogel to the injured tendon, thus providing long-term mechanical support to the tendon. In addition, the hydrogels exhibited universal adhesion properties in the complex environment of the hydrogel–tendon interface (Supplementary Fig. 6G, H), adhering to different substrates and rat viscera and resisting the corresponding gravitational forces. Dynamic tests (Supplementary Fig. 6I) revealed that the hydrogels adhered to the pig skin surface and remained stable after bending, twisting, washing, and inversion.

In conclusion, HAPP hydrogels exhibited excellent self-healing, injectable, adaptive, and wet adhesion properties. Their self-healing properties maintained the integrity of the hydrogel through dynamic bond reorganization. Injectability and adaptability enabled minimally invasive precision implantation and filler adaptation. High-strength wet adhesion provided the basis for effective long-term mechanical support. Therefore, this approach demonstrates great potential for postoperative tendon repair.

Construction and characterization of Janus hydrogels with asymmetric adhesion

The excellent wet adhesion properties of hydrogels are significant for postoperative tendon repair, but potential nonspecific adhesion may trigger ectopic adhesion to surrounding tissues such as fascia, and this paradoxical need makes precise modulation of asymmetric adhesion an important issue in the application of hydrogels for tendon repair[43]. As shown in Fig. 4A, HAPP hydrogels were used to achieve asymmetric adhesion (wet adhesion on the side of the tendon and antiadhesion on the side of the LLP) by incorporating polyethylene (PE)-based lotus leaf moulds (LPPs), which might be explained mainly by the following mechanisms[20,44,45]. First, on the tendon side, the hydrogel precursor injected into the LLP seamlessly joined with the tissue and formed extensive and strong forces such as hydrogen bonding through its micromobility and disruption of the hydration layer at the tissue interface via in-migration of its polar group. On the LLP side, the superhydrophobicity of the lotus leaf surface induced microinternal migration of the polar groups of the polymer chains at the hydrogel interface while the fat chains were exposed to the surface. Furthermore, the high-strength covalent bonds formed by UV cross-linking maintained the distribution of polar groups and fat chains, resulting in the formation of a hydrophobic interface with a small number of polar groups and a large proportion of fat chains on the LLP side and, simultaneously, stabilizing the strong adhesion force on the tendon side. This dual theoretical basis of “in-migration-locking” provided a solid foundation for the realization of asymmetric adhesion. The mechanism was further verified via energy dispersive spectroscopy (EDS). After LLP treatment, the signal of carbon on the hydrogel surface increased, whereas the signals of oxygen and nitrogen decreased. The main polar groups in the HAPP hydrogels included hydroxyl groups, amino groups, and carboxyl groups. This finding indicated that some of the polar groups in the hydrogel migrated inwards and that the aliphatic chain segments moved upwards after LLP treatment, which was consistent with our previous speculation (Supplementary Fig. 16).

To verify whether asymmetric adhesion of the hydrogel was successfully induced, LLP was wrapped around isolated rat Achilles tendons after injection of HAPP3 precursor solution, which was subsequently cured by UV cross-linking, after which the LLP was removed, wrapped with pigskin, and added to the outer layer of the hydrogel. Finally, tensile testing was performed while the same contact area was maintained on both sides (Fig. 4B). Unexpectedly, the hydrogel–pigskin interface in the OAR (outer-surface antiadhesive remoulding) group peeled off before the hydrogel–tendon interface. The data analysis revealed that in the WR (without remoulding) group (Fig. 4C), the shedding strength of the hydrogel–tissue interface was greater than 27.62 ± 0.87 kPa in all the groups, which was generally consistent with the results of the lap–shear test. In the OAR group (Fig. 4D), the shedding strength of the hydrogel–pig skin interface was only 4.32 ± 0.27 kPa (HAP), 4.87 ± 0.24 kPa (HAPP1), 5.45 ± 0.33 kPa (HAPP2), 5.94 ± 0.31 kPa (HAPP2), and 6.33 ± 0.29 (HAPP4), which was 5.53 ~ 6.39 times lower than that of the WR group. The contact angle test revealed (Fig. 4C, D) that after 120 ms of contact, the surface contact angle of the WR group was only 40°, whereas the surface contact angle of the OAR group was as high as 89°. The asymmetric adhesion properties of the hydrogels were verified by cell experiments. The HAPP3 hydrogels were placed in six-well plates as a cell culture substrate; one group was left untreated, and the other group was treated with LLP (Fig. 4E). The schematic of cell adhesion at different interfaces of the hydrogel is shown in Fig. 4F. The results (Fig. 4H) revealed that the cell adhesion rate of the OAR group was only 17.96 ± 4.46% of that of WR group. Immunofluorescence staining (Fig. 4G) revealed that the cytoskeleton of the OAR group was round or pike shaped and that the adhesion area to the hydrogel substrate was small, whereas the cells of the WR group had more pseudopods and a larger adhesion area. Quantitative analysis revealed (Fig. 9I, J) that the mean cell spread area and mean cell perimeter of the OAR group were only 33.49 ± 9.85% and 43.87 ± 8.32% of those of the WR group, respectively. In addition, the cell adhesion-associated proteins F-actin, FN, and Col 1A1 and the antiadhesion-associated protein MMP9 were detected by Western blot analysis[46–48]. The results (Fig. 4K) revealed that the expression of the adhesion-associated proteins F-actin, FN, and Col 1A1 was lower in the OAR group than in the WR group and that the expression of the antiadhesion-associated protein MMP9 was greater in the OAR group than in the WR group. The above experiments demonstrated the successful induction of asymmetric adhesion to Janus hydrogels at the physical–cellular–molecular level and confirmed the excellent cytocompatibility of HAPP3 hydrogels. This dual combination of interface-induced network reconfiguration and UV covalent cross-linking locking allowed for better stability of asymmetric adhesion constructs in vivo. This design could act as a physical barrier to prevent cell and protein adhesion and suppress the inflammatory response and fibrosis[20,44,45].

Spatiotemporal modulation of bacterial infection by the hydrogels

Bacterial capture kinetic tests (Fig. 5A, B) revealed that the hydrogels had capture efficiencies of 28.24 ± 3.31% (HAP), 28.91 ± 2.86% (HAPP1), 29.34 ± 2.79% (HAPP2), 29.93 ± 2.11% (HAPP3), and 30.25 ± 2.54% for MRSA within 60 min. The trend of the capture rates for *E. coli* and *S. aureus* was consistent with that for MRSA. The capture mechanism of the hydrogels was based mainly on the formation of phenyl borate bonds between the phenyl borate groups in the HAPP hydrogel system and the diol groups in the bacterial cell

https://doi.org/10.1038/s41467-026-68514-0

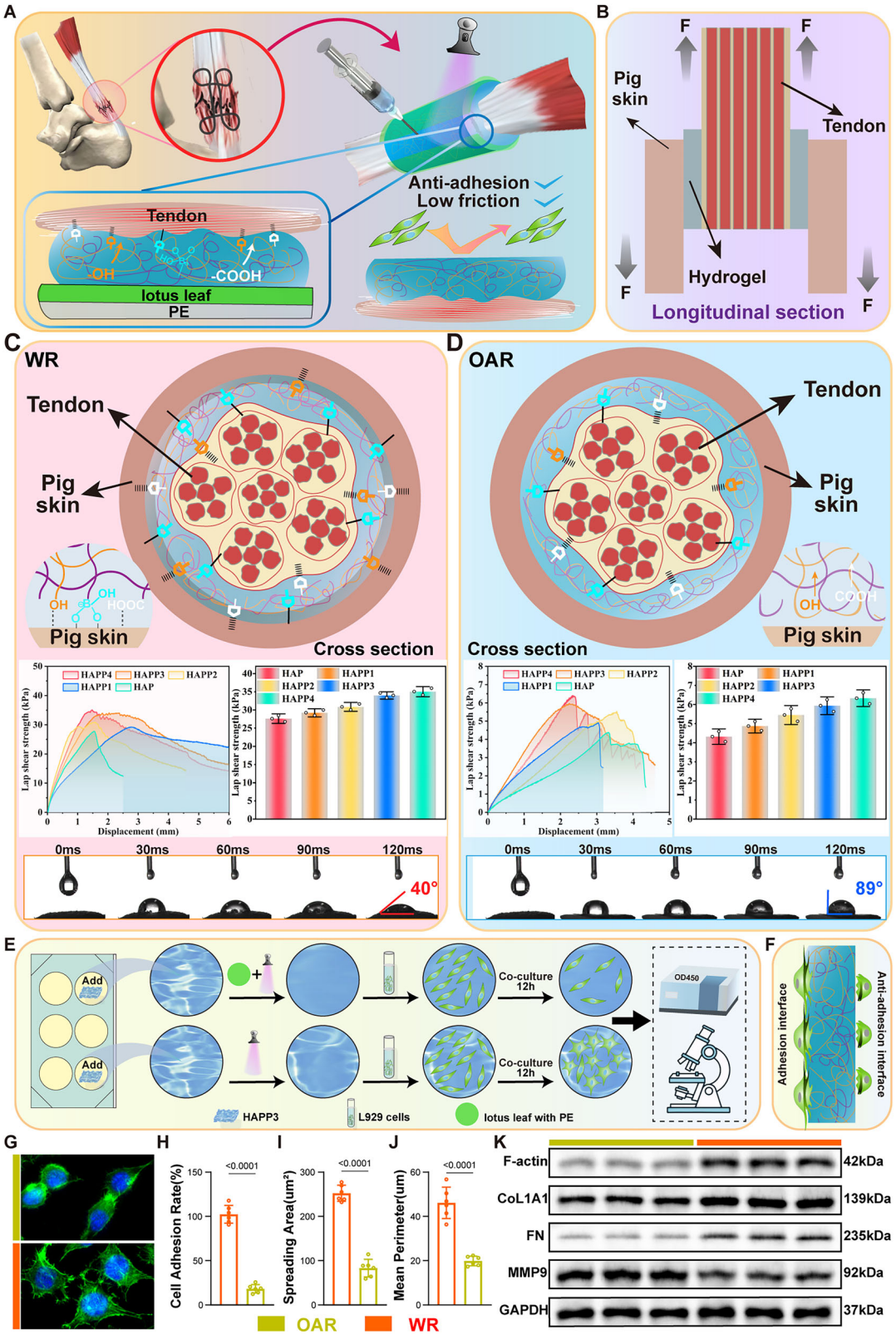

Fig. 4 | Construction and characterization of Janus hydrogels to achieve asymmetric adhesion. A Schematic diagram of the construction of the hydrogel to achieve asymmetric adhesion. **B** Schematic longitudinal cross section of the lap-shear test for asymmetric adhesion. **C**, **D** Schematic cross-section of the lap-shear test of the hydrogel, molecular details of the adhesion to pig skin, adhesion strength statistics ($n = 3$), and contact angle test ($n = 3$). OAR: Outer-surface anti-adhesive remoulding. WR: Without remoulding. **E** Schematic diagram of the cell adhesion process. **F** Detailed view of cells adhering to different interfaces of the hydrogel. **G** L929 cytoskeleton staining. **H** Cell adhesion rate ($n = 6$). **I** Cell Spreading area ($n = 5$). **J** Cell mean perimeter ($n = 5$). **K** WB bands. The data in (**H**–**J**) were analysed by one-way ANOVA to determine statistical significance. (n values derived from different experimental units. The data are presented as the mean ± standard deviation (SD). The (**H**–**J**) statistical significance was determined by one-way ANOVA).

https://doi.org/10.1038/s41467-026-68514-0

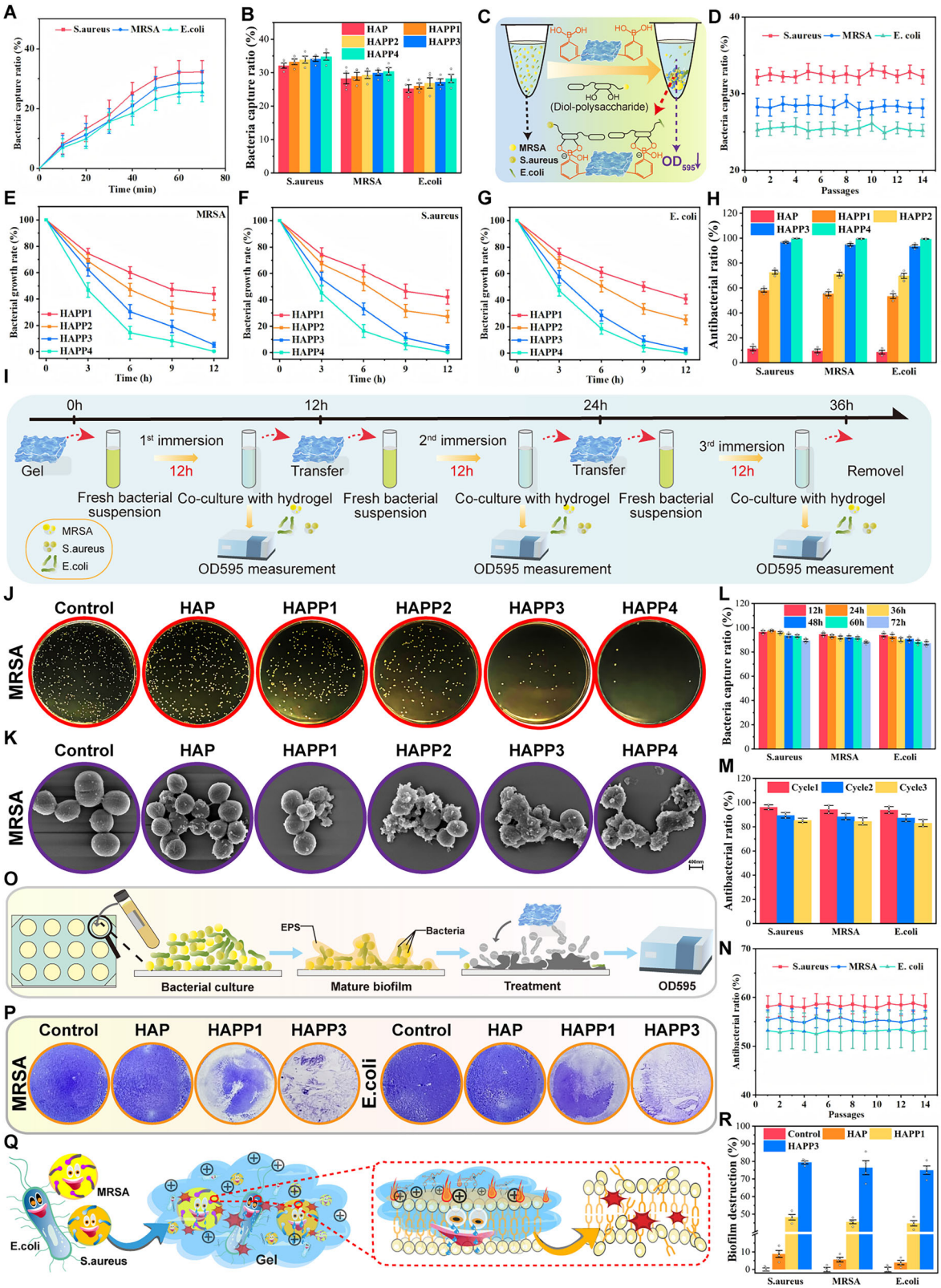

Fig. 5 | Spatiotemporal antibacterial effects of the hydrogels. A Quantitative graph of the bacterial capture rate ($n = 4$). **B** Statistical graph of the bacterial capture rate ($n = 4$). **C** Schematic diagram of the bacterial capture mechanism. **D** Graph of the bacterial capture resistance test ($n = 5$). **E** Bactericidal kinetic graphs for (MRSA), **F** *S. aureus*, and **G** *E. coli*. **H** Statistical graph of the sterilization rate ($n = 3$). **I** Schematic diagram of the process of repeated sterilization experiments. **J** Macroscopic antimicrobial physical diagram. **K** Bacterial FE-SEM image. **L** Long-term sterilization statistics ($n = 3$). **M** Repeated sterilization statistics ($n = 3$). **N** Bacterial resistance detection curve ($n = 4$). **O** Schematic diagram of the process of the antibiofilm experiment. **P** Macroscopic image of crystal violet staining. **Q** Schematic diagram of the bactericidal mechanism. **R** Statistical graph of the antibiofilm test results ($n = 4$) (n values derived from different experimental units. The data are presented as the mean ± standard deviation).

wall polysaccharides (Fig. 5C)[13]. The differences between the groups might be related to the increased content of PEI, which has many amino-positive groups that can physically adsorb some bacteria through electrostatic interactions[49]. This experiment confirmed the excellent spatial localization and capture ability of the hydrogels against bacteria. The adaptive evolution of the three bacteria to the effects of the HAP hydrogel was subsequently assessed by successive 14-generation cultures. The results (Fig. 5D) revealed that the capture rate of MRSA was consistently maintained at approximately 28.33 ± 0.27%, the capture rate of *S. aureus* fluctuated at approximately 32.45 ± 0.32%, and the capture rate of *E. coli* was stable at approximately 25.40 ± 0.29%. No significant evolution of bacterial capture resistance to the hydrogels was observed in the experiments, which confirmed that the trapping mechanism of the phenylborate bond did not easily induce bacterial capture resistance.

The bactericidal kinetics of the HAPP hydrogels against *E. coli*, *S. aureus*, and MRSA were evaluated by optical density (OD) dynamic monitoring (Fig. 5E–G). The results revealed that the HAPP3 and HAPP4 groups exhibited rapid and sustained bactericidal effects against all three types of bacteria. The bactericidal rates of HAPP3 were 43.62 ± 2.91% (MRSA), 42.37 ± 2.68% (*E. coli*), and 44.18 ± 3.18% (*S. aureus*) at 3 h. The bactericidal rates at 12 h reached 94.66 ± 2.54% (MRSA), 93.39 ± 2.63% (*E. coli*), and 96.06 ± 2.24% (*S. aureus*), respectively. These results confirmed the excellent chronodynamic bactericidal properties of the HAPP hydrogels. The spread plate method revealed that after the bacteria were cocultured with the HAPP hydrogel for 12 h, the number of colonies on the plates gradually decreased with increasing PEI content in the hydrogel (Fig. 5J, Supplementary Fig. 7A). Quantitative analysis revealed that the antimicrobial rate of the hydrogel increased with increasing PEI concentration (Fig. 5H) and reached 94.76 ± 1.97% (MRSA), 93.51 ± 2.35% (*E. coli*), and 96.74 ± 1.25% (*S. aureus*) in the HAPP3 group. Field emission scanning electron microscopy (FE-SEM) was subsequently used to observe the bacteria cocultured with the hydrogel for 12 h (Figs. 4K, S7B), revealing that the bacteria in the control group were morphologically intact, with smooth surfaces, that the MRSA and *S. aureus* bacteria were spherical and that the *E. coli* bacteria were rod shaped. In contrast, in the HAPP3 and HAPP4 groups, the cell membranes of MRSA, *S. aureus*, and *E. coli* were largely ruptured, and the intracellular contents were leaked.

Long-term antimicrobial experiments revealed (Fig. 5L) that the antimicrobial rates of the HAPP3 hydrogels reached as high as 88.08 ± 2.88% (MRSA), 87.19 ± 2.93% (*E. coli*), and 89.51 ± 3.51% (*S. aureus*) at 72 h, which might be related to the sustained trapping ability of the phenylboronic acid moiety in the system and the sustained disruption of bacterial cell membranes by PEI[13]. Furthermore, the results of a repeatability test (Figs. 5I and 5M) revealed that the bactericidal efficiency of the HAPP3 hydrogel was 84.47% ± 3.02% (MRSA), 83.14 ± 3.92% (*E. coli*), and 85.35 ± 2.79% (*S. aureus*) after 3 cycles, which coincided with the long-lasting antimicrobial activity of the hydrogel. Successive 14-generation cultures were performed to evaluate the resistance of the three bacteria to the HAPP1 hydrogel, and the results (Fig. 5N) revealed that the antibacterial rates of MRSA, *E. coli*, and *S. aureus* were consistently stable at 55.36 ± 0.35%, 53.11 ± 0.25%, and 58.37 ± 0.30% (P0–P14), respectively, with no significant decreasing trend.

During colony formation, bacteria form complex and dense biofilms, which are highly resistant to the penetration of conventional antibiotics, thus severely affecting the effectiveness of antimicrobial treatment[50]. Crystal violet staining (Fig. 5P, Supplementary Fig. 7C) revealed that the biofilms in the control group remained structurally intact, whereas the biofilms treated with the HAPP hydrogel presented a reduction in biomass. Among them, HAPP3 showed excellent biofilm removal ability, almost completely destroying the dense membrane structure. The quantitative results (Fig. 5R) revealed that the biofilm biomass gradually decreased with increasing PEI content. This phenomenon might be due to the introduction of PEI, which disrupted the biofilm by destroying extracellular polymeric substances (EPSs), key bacterial secretions within the biofilm that evade the immune system (Fig. 5O)[51]. However, the specific antibiofilm mechanism still needs further research and exploration.

In conclusion, the HAPP hydrogel efficiently killed MRSA, *E. coli*, and *S. aureus* through its spatiotemporally synergistic "capture-physical membrane-breaking" mechanism (Fig. 5Q) and effectively disintegrated the biofilm. These characteristics provided an innovative solution for the spatiotemporal modulation of bacterial activity and drug resistance in drug-resistant bacterium-infected injured tendons.

Biocompatibility

L929 cells were cocultured with the HAPP hydrogel extract and lotus leaf extract for 12 h, 24 h, and 48 h, after which the live and dead cells were stained (Supplementary Fig. 8A). Compared with the blank control group, the HAPP4 group presented a smaller number of viable cells and a larger number of dead cells; however, the results of the other hydrogel and lotus leaf groups did not significantly differ. These findings suggested that all of the lotus leaf and hydrogel groups possessed excellent cytocompatibility, but the introduction of too much PEI might have caused some cytotoxicity. The haemolysis results (Supplementary Fig. 8B) revealed that the haemolysis rate of the ultrapure water treatment group was close to 100%, while the haemolysis rates of all the groups of hydrogels were significantly lower than 5%, with the highest haemolysis rate observed for HAPP4. Owing to the complexity of the in vivo environment, the histocompatibility was further verified by subcutaneous implantation of HAPP3 hydrogels in rats. H&E staining (Supplementary Fig. 8C) revealed that key organs, such as the heart, liver, spleen, lungs, and kidneys, were intact after 3 months of implantation, and no abnormal lesions were detected. As shown in Supplementary Fig. 9, live imaging revealed that on day 7 after implantation of the HAPP3 hydrogel at the Achilles tendon site in mice, distinct fluorescence signals were observed at the implantation site and uniformly distributed throughout the surgical area. As time progressed, both the fluorescence intensity and the distribution range gradually decreased, and the fluorescence signals completely disappeared by postoperative day 35, indicating that the hydrogel was progressively degraded and cleared by the in vivo microenvironment. This result confirmed its controllable degradability and in vivo biocompatibility. The above experiments demonstrated the excellent biocompatibility and long-term safety of the materials used, providing a strong guarantee for their safe application in clinical scenarios such as trauma repair and tissue engineering.

On the basis of the results of the experiments, the Janus hydrogels prepared in this study possessed the mechanical adaptability and asymmetric adhesion ability of biomimetic tendon sheaths, as well as excellent broad-spectrum antimicrobial properties. Among them, HAPP3 and HAPP4 were superior in terms of their mechanical and antimicrobial properties. On the basis of the possible cytotoxicity of HAPP4, HAPP3 was chosen as a carrier to carry exosomes for subsequent experimental studies.

Identification of cells, exosomes, and pH-responsive controlled release of exosomes. Hypo-TDSCs extracted from rat Achilles tendon tissues were cultured in a hypoxic environment to obtain Hypo-TDSCs. The cells were subsequently characterized to ensure the quality and specificity of the extracted exosomes. Light microscopy revealed that the cells were typically spindle shaped or shuttle shaped (Supplementary Fig. 10A). Flow cytometry analysis (Supplementary Fig. 10B) revealed positive staining for the MSC-associated markers CD90 and CD44 but negative staining for the negative markers CD45 and CD11b, confirming the successful extraction of TDSCs and Hypo-TDSCs[52].

https://doi.org/10.1038/s41467-026-68514-0

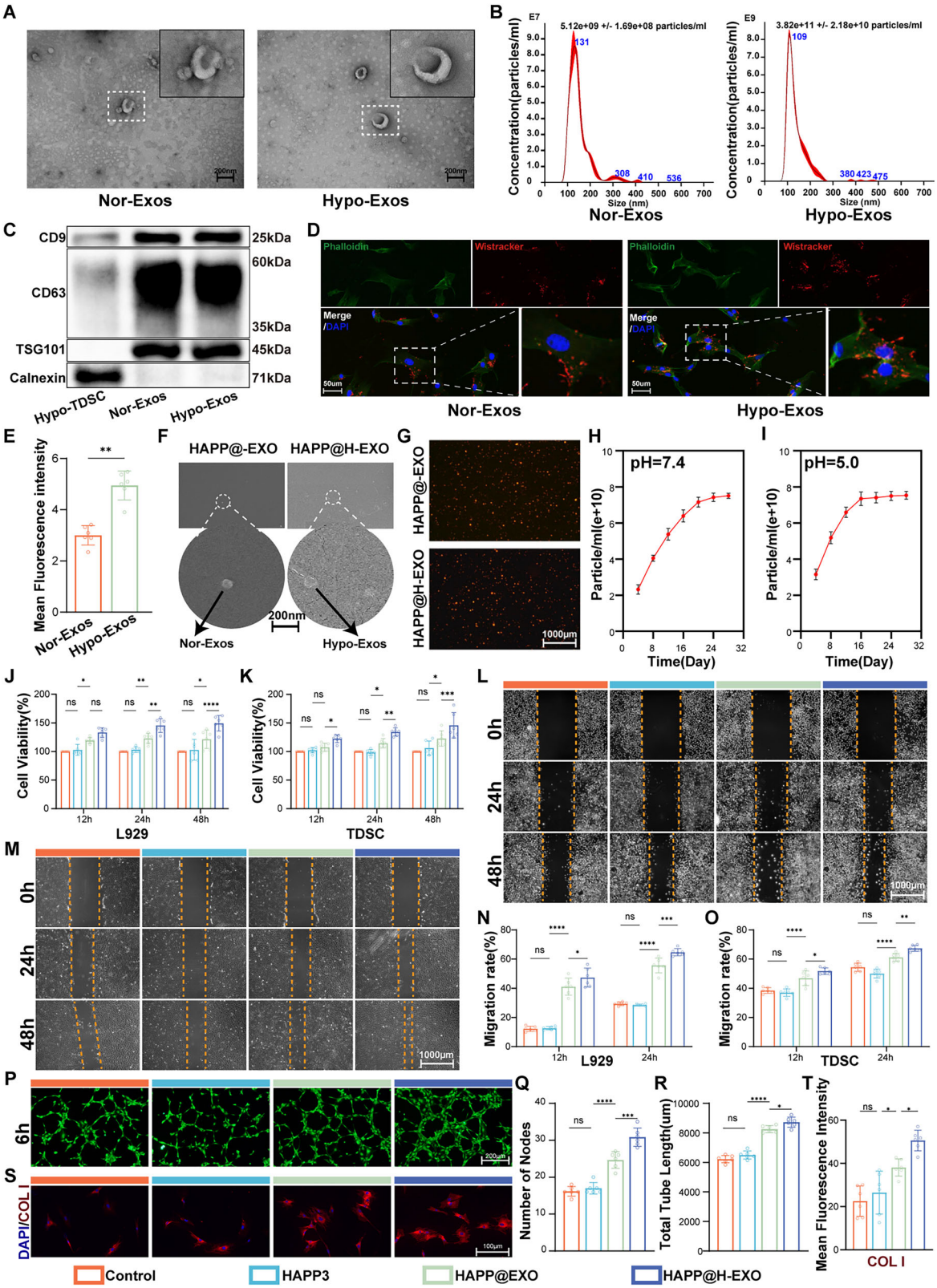

Exosomes were extracted from two different cell culture supernatants by differential ultracentrifugation. Transmission electron microscopy (TEM) revealed that both Nor-Exos and Hypo-Exos had a typical exosome spherical bilayer membrane structure with a diameter of approximately 150 ± 20 nm (Fig. 6A). Nanoparticle analysis (NTA) revealed (Fig. 6B) that the particle size of both Nor-Exos and Hypo-EXOs was approximately 150 ± 100 nm, but the concentration of Hypo-Exos ($3.82 \times 10^{11} \pm 2.18 \times 10^{10}$ particles/mL) was greater than that of Nor-Exos ($5.12 \times 10^{9} \pm 1.69 \times 10^{8}$). In addition, Western blot analysis revealed distinct bands for exosome-specific markers (CD9, CD63, and TSG101), and calnexin was expressed only in Hypo-TDSCs (Fig. 6C). These results were consistent with those of previous studies on exosomes[53] and demonstrated that hypoxic preconditioning significantly increased exosome secretion. The exosome uptake assay

Fig. 6 | Characterization of exosomes and in vitro biological functions of HAPP@H-EXO. A TEM image of exosomes. **B** NTA of exosomes. **C** Western blot analysis of CD9, CD63, TSG101, and calnexin expression. **D** Immunofluorescence of internalized exosomes (Wistracker) from TDSCs. **E** Quantification of Wistracker fluorescence intensity. **F** FE-SEM images of HAPP@H-EXO and HAPP@EXO. **G** Wistracker-labelled exosomes were uniformly embedded in the hydrogels. **H** Slow-release curves of exosomes at **H** pH = 7.4 and **I** pH = 5.0. Cell proliferation rates of **J** L929 cells and **K** TDSCs. **L** Scratch assay of **L** L929 cells and **M** TDSCs. **N** Quantification of the mobility of **N**L929 cells and **O** TDSCs. **P** HUVEC in vitro tube-forming images. **Q** Number of nodes associated with HUVEC tube formation with **R** total branch length. **S** Immunofluorescence images of COL1 in TDSCs and **T** quantification of fluorescence intensity ($n = 6$. n values derived from different experimental units. The data are presented as the mean ± standard deviation. The E statistical significance was determined by one-way ANOVA, The (**J**–**K**), (**N**–**O**), (**Q**–**T**) statistical significance was determined by multiway ANOVA).

results (Fig. 6D) revealed that Wistracker-labelled exosomes could be internalized into the intracellular compartments of TDSCs, confirming their ability to deliver active components into the cells. Notably (Fig. 6E), quantitative fluorescence analysis revealed that the uptake rate of Hypo-Exos was greater in TDSCs than in control TDSCs, suggesting that hypoxic preconditioning might further enhance the biological efficacy of exosomes by increasing their secretion and internalization efficiency.

The two types of exosomes were loaded in hydrogels to form HAPP@H-EXO and HAPP@EXO, as described in the 'Methods' section. FE-SEM directly revealed that the exosomes were encapsulated in the hydrogel, which remained round in shape, and that their diameter did not change significantly (Fig. 6F). Moreover, fluorescence microscopy revealed that the Wistracker-labelled exosomes were uniformly distributed inside HAPP3 (Fig. 6G), confirming that the exosomes were successfully loaded into the HAPP3 hydrogel. The release behaviour of the exosomes was mainly controlled by the degradation of the hydrogel, and the degradation time of HAPP3, which was greater than 24 days, facilitated local retention and long-term stable release of the exosomes. The exosome release curve revealed that the exosomes were completely released in PBS at pH = 7.4 on the 24th day, which was essentially consistent with the hydrogel degradation curve (Fig. 6H, Supplementary Fig. 11A). In PBS at pH 5, the exosomes were completely released on the 16th day (Fig. 6I, Supplementary Fig. 11B). This phenomenon might be attributed to the pH-responsive dissociation of dynamic borate bonds within HAPP3[34]. This difference in pH-responsive release allowed rapid release in the acidic microenvironment during the preinjury phase to rapidly modulate the inflammatory response and slower release during the postinjury phase as the pH returned to neutral to promote regeneration and repair of the tendon tissue.

HAPP@H-EXO promotes cell proliferation, migration, tube formation, and differentiation

HUVECs and L929 cells are endothelial and fibroblast lines, respectively, and are widely used in experimental studies of cell proliferation, migration, and angiogenesis in vitro[26,54]. A CCK8 assay of L929 cells and TDSCs (Fig. 6J, K) revealed that HAPP3 did not significantly promote cell proliferation, whereas both HAPP@EXO and HAPP@H-EXO showed excellent proliferation-promoting ability, with the latter exhibiting better performance. A scratch wound healing assay (Fig. 6L-O) revealed that there was no significant difference between the HAPP3 and control groups, and the HAPP@EXO and HAPP@H-EXO groups significantly promoted cell migration, whereas the migration rate was greater in the HAPP@H-EXO group. An angiogenesis assay of HUVECs in vitro revealed that the HAPP@H-EXO group presented the best tube-forming performance among the four groups, with the number of tube-forming junctions reaching 30.83 ± 3.50 (vs. control, $p < 0.001$), and the total length reached 8725.14 ± 507.11 mm (vs. control, $p < 0.05$). More importantly, immunofluorescence staining of TDSCs (Fig. 6S, T) revealed that compared with the HAPP@H-EXO group, the HAPP@EXO and HAPP@H-EXO groups showed significantly increased expression of COL I, which was 1.328 times greater in the HAPP@EXO group. These results suggested that the addition of Hypo-Exos greatly enhanced the ability of HAPP3 to promote cell proliferation, migration, and angiogenesis and could promote the differentiation of TDSCs into tendon cells, resulting in promising potential for the repair of tendon injuries in particular.

HAPP@H-EXO scavenges ROS and regulates the immune response

The combined effect of drug-resistant bacterial biofilms and the ischaemic microenvironment in the environment of infected tendon injury results in the sustained release and accumulation of ROS, leading to the collapse of the mitochondrial membrane potential of tendon cells, which in turn impedes the repair process of the injured tendon[50,55]. TDSCs were treated with HAPP3, HAPP@EXO, or HAPP@H-EXO after H_2O_2-induced oxidative stress. ROS fluorescence and quantitative analyses (Fig. 7A, C) revealed that H_2O_2 stimulation significantly elevated intracellular ROS levels, whereas ROS accumulation was significantly inhibited by HAPP@EXO and HAPP@H-EXO treatment, and the effect of HAPP@H-EXO was more significant (vs. HAPP@EXO, $p < 0.01$). A mitochondrial membrane potential (MMP) assay further revealed (Fig. 7B, D) that H_2O_2 led to severe depolarization of the MMP (a decrease in the red/green fluorescence ratio), whereas compared with HAPP@EXO, HAPP@H-EXO effectively restored the MMP, revealing a significant increase ($p < 0.0001$).

The immune microenvironment after infectious tendon injury is intensely proinflammatory, with high M1 macrophage polarization and inflammatory factor secretion and limited M2 macrophage polarization due to a low blood supply, leading to a vicious cycle of inflammation and prolonged healing at the site of tendon injury[18,23]. Immunofluorescence staining revealed (Fig. 7E–H) that lipopolysaccharide (LPS) significantly upregulated the proinflammatory M1 marker INOS, confirming the successful induction of M1 macrophage polarization. Moreover, no significant anti-inflammatory effects were observed after HAPP3 treatment, whereas INOS expression was decreased and CD206 expression was increased in response to HAPP@EXO treatment, confirming that the anti-inflammatory effects of HAPP@EXOs were dependent mainly on TDSC-EXOs. However, whether the hydrogel has a synergistic effect still requires further independent research in the future. Notably, HAPP@H-EXO treatment resulted in lower INOS expression (vs. HAPP@EXO, $p < 0.001$) and increased CD206 signalling intensity (vs. HAPP@EXO, $p < 0.0001$), suggesting that hypoxic preconditioning enhanced the anti-inflammatory effects of the exosomes. ELISA (Fig. 7, J, Supplementary Fig. 11C, D) revealed that after 72 h of coculture, secretion of the inflammatory factor IL-6 was reduced by 34.53% (vs. that in the LPS group, $p < 0.01$), and the level of the anti-inflammatory factor IL-10 was elevated by 1.44-fold (vs. that in the LPS group, $p < 0.0001$) in HAPP@H-EXO-treated cells. These findings further confirmed that HAPP@H-EXO could regulate the immune microenvironment.

To analyse the mechanism by which HAPP@H-EXO inhibited inflammatory responses by regulating macrophage polarization, mRNA-seq was performed on macrophages in the LPS and LPS + HAPP@H-EXO groups (Supplementary Fig. 12). Volcano plot analysis (Fig. 7K) revealed 5772 differentially expressed genes (DEGs) (log2FC > 1, FDR < 0.05). Differential gene heatmap analysis (Fig. 7L) revealed that anti-inflammatory regulators (e.g., IL10, NFKBIA, and IL1RN), antioxidative stress regulators (e.g., SOD2 and FOXO3), and cell proliferation and differentiation regulators (e.g., NRAS and BRAF) were significantly upregulated. GO enrichment analysis (Fig. 7M) revealed

https://doi.org/10.1038/s41467-026-68514-0

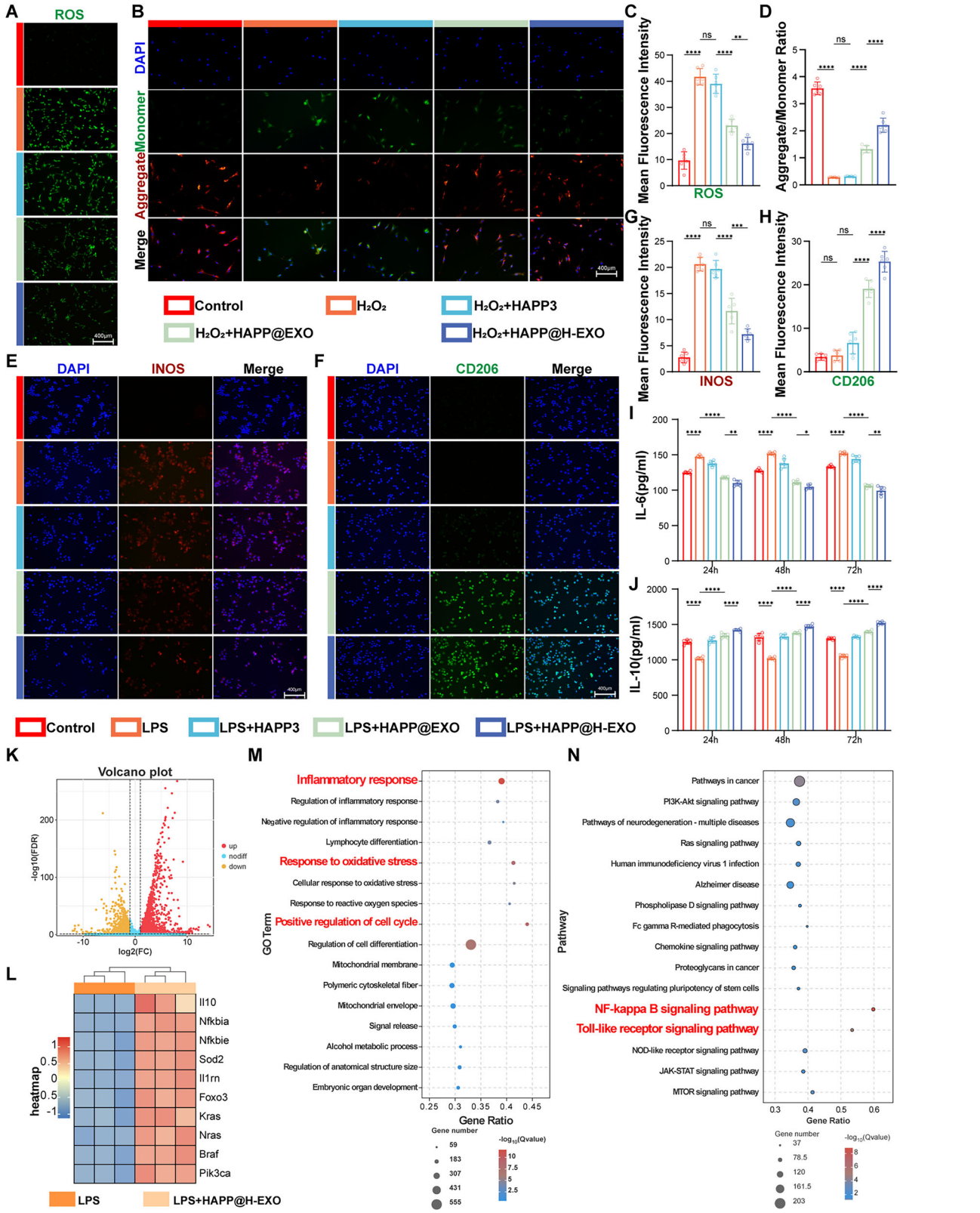

Fig. 7 | HAPP@H-EXO scavenges ROS and regulates the immune response. **A** Fluorescence staining images of ROS and **C** quantification of the fluorescence intensity of TDSCs. **B** Fluorescence staining of the mitochondrial membrane potential of TDSCs and **D** quantification of fluorescence intensity. **E** INOS immunofluorescence image of RAW264.7 cells and **G** quantification of fluorescence intensity. **F** Immunofluorescence image of CD206 from RAW264.7 cells and **H** quantification of fluorescence intensity. **I** Statistical plots of the ELISA results for IL-6 and **J** IL-10. **K** Volcano plot of the mRNA-seq data. **L** Heatmap of differentially expressed genes. **M** GO enrichment analysis. **N** KEGG enrichment analysis ($n = 6$ in the (**C**, **D**), (**G**, **H**), and (**I**, **J**), $n = 3$ in the (**K**–**N**), n values derived from different experimental units. The data are presented as the mean ± standard deviation. The (**C**, **D**), (**G**, **H**), and (**I**, **J**) statistical significance was determined by multiway ANOVA).

that the DEGs were significantly associated with the biological processes "inflammatory response," "positive regulation of the cell cycle," and "response to oxidative stress" (FDR < 0.05). KEGG pathway analysis further revealed that HAPP@H-EXO might interfere with mainly the NF-κB signalling pathway (p = 1.07E-11) and the Toll-like receptor signalling pathway (p = 8.10E-8). Further verification via Western blotting (Supplementary Fig. 17) revealed that HAPP@H-EXO significantly inhibited the phosphorylation of P65 and IκB-α, which are key effector molecules in the NF-κB pathway[56]. This finding was consistent with the results of the in vitro macrophage phenotype rescue experiment, confirming that HAPP@H-EXO reprogrammed macrophages by inhibiting the NF-κB pathway and driving M2 polarization. The above results further confirmed that HAPP@H-EXO protected TDSCs by scavenging ROS and maintaining mitochondrial function and might also drive macrophage polarization towards the anti-inflammatory M2 phenotype and the secretion of anti-inflammatory factors through the inhibition of signalling pathways such as the NF-κB pathway. This feature provided a dual-targeted "antioxidative stress–anti-inflammatory" therapeutic strategy for the repair of infected tendons.

In vivo antimicrobial and anti-inflammatory effects of HAPP@H-EXO

On the basis of the encouraging results showing that HAPP@H-EXO promoted cell proliferation, migration, and differentiation, as well as anti-inflammatory and antioxidative stress in vitro, we further validated the in vivo therapeutic efficacy of HAPP@H-EXO by constructing a rat model of MRSA infection after Achilles tendon rupture surgery. A schematic of the healing timeline after surgical modelling, immune response analysis, histological analysis, electron microscopy analysis, behavioural analysis, and mechanical analysis is shown in Fig. 8A. Supplementary Fig. 13 presents real-object photographs of the construction process for both the LLP mould and the animal model establishment process.

Figure 8B shows a schematic diagram of the in vivo antimicrobial, antioxidative stress, and anti-inflammatory therapeutic effects of HAPP@H-EXO. Samples were collected on the 3rd day and 1st week after surgery for MRSA culture analysis. The results (Fig. 8C) revealed that on day 3, many bacterial colonies were cultured from the tissues of the infection group, and a small number of bacterial colonies were found in the Inf-HAPP3, Inf-HAPP@EXO, and Inf-HAPP@H-EXO groups. At the 1st week, many bacterial colonies were still present in the tissues of the infection group, whereas essentially no bacterial colonies were found in the Inf-HAPP3, Inf-HAPP@EXO, or Inf-HAPP@H-EXO groups. As shown by quantitative analysis (Supplementary Fig. 14), when the infection group was used as a control, the antimicrobial rates on the 3rd day reached 96.93 ± 0.718% (Inf-HAPP3), 96.58 ± 1.088% (Inf-HAPP@EXO), and 96.23 ± 0.582% (Inf-HAPP@H-EXO), and those on the 1st week reached 98.38733 ± 0.73% (Inf-HAPP3), 98.03208 ± 1.10% (Inf-HAPP@EXO), and 97.67683 ± 0.59% (Inf-HAPP@H-EXO), respectively. These findings demonstrated the strong anti-infective ability of HAPP@H-EXO, which was consistent with the in vitro antimicrobial performance test.

The in vivo antioxidative stress and anti-inflammatory properties of HAPP@H-EXO were analysed by electron microscopy and immunofluorescence staining of samples collected 2 weeks after surgery. Electron microscopy (Fig. 8D) revealed that the mitochondria in the infection group were swollen and deformed, the outer membrane was damaged, and the mitochondrial cristae were incomplete, resulting in a more disorganized appearance. After treatment with HAPP@H-EXO and HAPP@H-EXO, the mitochondria were slightly swollen, the tubular cristae were preserved, and the integrity of the mitochondrial cristae and outer membrane improved to a greater extent in the HAPP@H-EXO group, which presented normal mitochondrial morphology. ROS fluorescence staining and quantitative analysis revealed (Fig. 8E, F) that the infection group presented the highest level of red ROS fluorescence, whereas the Inf-HAPP@H-EXO group presented the lowest level of ROS, which was 66.12% lower than that of the infection group (p < 0.0001). CD86 and CD206 fluorescence (Fig. 8E, G–I) staining revealed that the red fluorescence of CD86 significantly decreased after HAPP@H-EXO treatment and was 71.68% lower than that of the infection group (P < 0.0001), whereas the green fluorescence of CD206 was significantly greater than that of the infection group (p < 0.0001), and the M2/M1 ratio increased from 0.18 ± 0.03 to 2.12 ± 0.84 (infection group vs. Inf-HAPP@H-EXO group, p < 0.0001). In addition (Fig. 8E, J, K), TGF-β expression was significantly upregulated in the Inf-HAPP@H-EXO group (vs. the infection group, p < 0.0001), and TNF-α expression was significantly decreased (vs. the infection group, p < 0.0001). The above results confirmed that HAPP@H-EXO could scavenge ROS and modulate inflammatory responses at an early stage, which was consistent with the results of the in vitro phenotyping experiments and analysis of the mRNA-seq results.

In conclusion, HAPP@H-EXO reprogrammed the microenvironment for continuous tissue remodelling and functional recovery at the early stage of infected tendon rupture repair through antimicrobial and anti-inflammatory effects.

HAPP@H-EXO promotes collagen sequential remodelling, vascularization, tendon regeneration, and stress redistribution

A schematic diagram of how hydrogel-released exosomes promote repair remodelling of tendon tissue is shown in Fig. 9A. The macroscopic and correlation staining maps of the 2 w and 6 w samples are shown in Fig. 9B. H&E and Masson's trichrome staining and data analysis revealed (Fig. 9C–G, P) that at the 2nd week, the infection group exhibited significant tissue vacuolization and collagen fibre disorganization, whereas treatment with HAPP@H-EXO reduced the formation of vacuole-like structures and promoted the deposition and orderly distribution of collagen fibres. At the 6th week, the collagen deposition and extracellular matrix regeneration of the Inf-HAPP@EXO and Inf-HAPP@H-EXO groups were still better than those of the infection group, with the Inf-HAPP@H-EXO group having the highest collagen volume fraction and regularity of arrangement. Notably, the Inf-HAPP@H-EXO group showed a clear gap between the tendon and the skin, whereas the infection group showed unclear boundaries between the tendon and the subcutaneous tissue and a disorganized structure. These findings suggested that the excellent performance of HAPP@H-EXO in preventing postoperative adhesions was consistent with the results of the in vitro experiments and the predicted results. This result was attributed mainly to the synergistic effect of Janus hydrogel construction and biological functions such as anti-inflammatory and antioxidant effects[57]. In addition, Sirius red staining revealed (Fig. 9H, Q) that the ratio of type I/III collagen fibres reached as high as 4.16 ± 0.20 after HAPP@H-EXO treatment, which was approximately 2.89-fold greater than that in the infection group. Furthermore, α-SMA fluorescence staining was performed on the 6-week samples, using the normal rat Achilles tendon group as the control. The results revealed that the infected group exhibited high levels of fluorescence expression. In contrast, the expression level in the HAPP@H-EXO treatment group was closest to that in the normal tissue group. These findings indicated that HAPP@H-EXO effectively promoted the orderly arrangement of tissue fibrosis without inducing abnormal excessive fibrosis (Supplementary Fig. 18).

Immunofluorescence staining of CD31 at 2 w revealed (Fig. 9I, R) that only a small amount of green CD31 fluorescence was detected in the infection group, whereas CD31 expression was significantly elevated after HAPP@EXO and HAPP@H-EXO treatment, and HAPP@H-EXO had a better proangiogenic effect. These findings indicated that HAPP@H-EXOs promoted vascular regeneration in tendon tissues, establishing essential nutrient transport channels for tissue healing at an early stage[58]. As they are core regulators of tendon cell development

https://doi.org/10.1038/s41467-026-68514-0

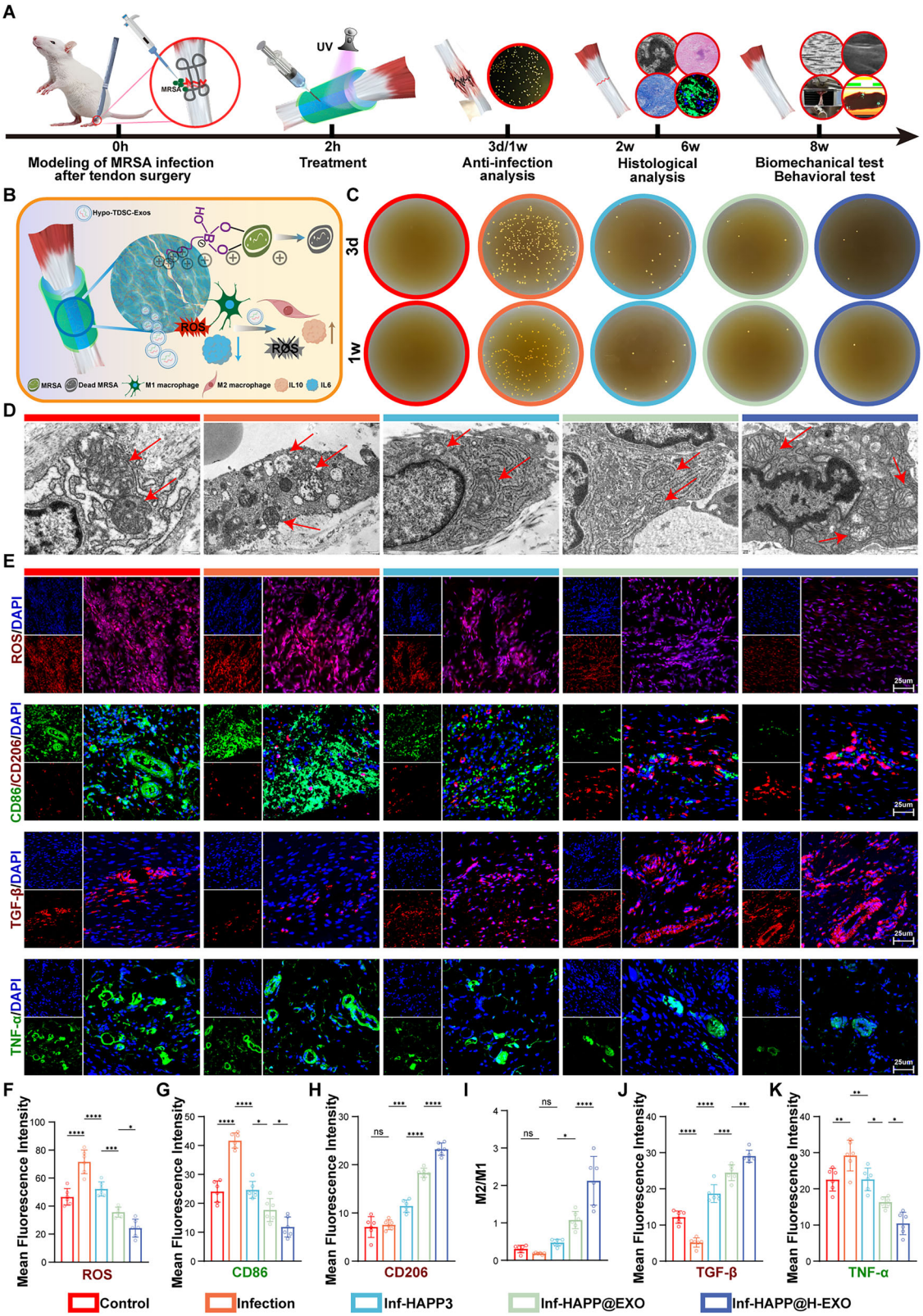

Fig. 8 | In vivo antimicrobial and anti-inflammatory effects of HAPP@H-EXO. **A** Schematic diagram of the animal experiment. **B** Schematic diagram of the in vivo antimicrobial, antioxidative stress, and anti-inflammatory therapeutic effects of HAPP@H-EXO. **C** Schematic of the in vivo antimicrobial effects. **D** TEM image of mitochondria. **E** Immunofluorescence staining for ROS, CD206, CD86, TGF-β, and TNF-α. **F** Quantitative fluorescence analysis of ROS levels. **G** Quantitative fluorescence analysis of CD86 expression. **H** Quantitative fluorescence analysis of CD206 expression. **I** Quantitative analysis of M2/M1 macrophages. **J** Quantification of TNF-α fluorescence. **K** Quantification of TGF-β fluorescence ($n = 6$, n values derived from different experimental units. The data are presented as the mean ± standard deviation. The statistical significance was determined by multi-way ANOVA).

https://doi.org/10.1038/s41467-026-68514-0

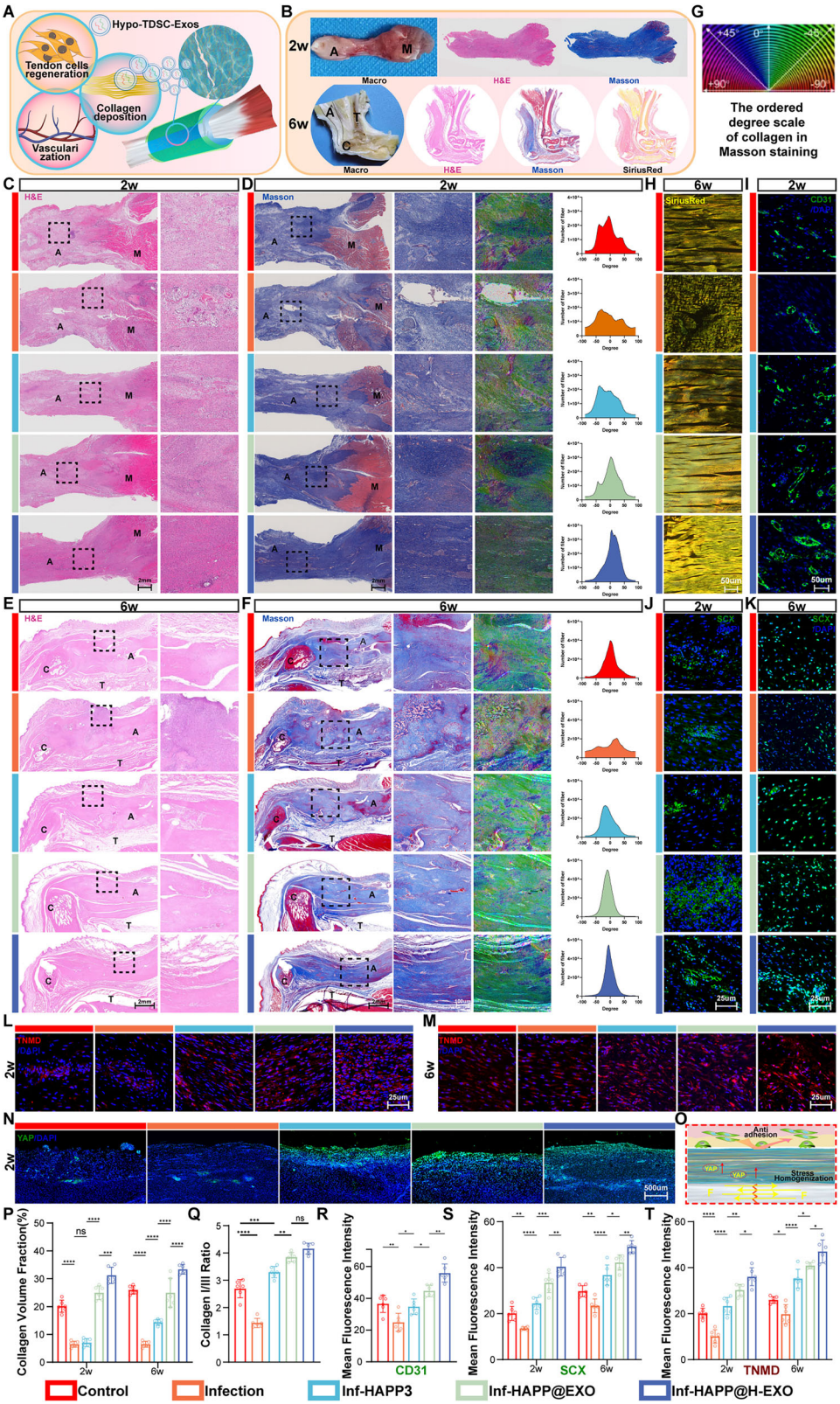

and maturation, the expression levels of tenomodulin (TNMD) and scleraxis (SCX) are closely related to the degree of functional regeneration of tendons[57]. Quantitative immunofluorescence analysis revealed (Fig. 9J–M, S, T) that the fluorescence intensity of TNMD and SCX in the HAPP@EXO and HAPP@H-EXO groups was significantly greater than that in the infection group at the 2nd week, and the expression intensity was even greater at the 6th week ($P < 0.001$). Notably, the expression of TNMD and SCX in the HAPP@H-EXO group was significantly greater than that in the HAPP@EXO group, suggesting that hypoxic preconditioning successfully enhanced the biological activity of the exosome and further strengthened its regulation of tendon regeneration and repair. YAP is a key protein involved in mechanical stress transduction[59,60]. Immunofluorescence staining (Fig. 9K, L) revealed that at the 2nd week, there was essentially no

Fig. 9 | HAPP@H-EXO promotes collagen sequential remodelling, vascularization, tendon regeneration, and stress redistribution. A Schematic illustration of the mechanism by which HAPP@H-EXO promotes collagen deposition, vascularization, and tendon cell regeneration. **B** Schematic of 2 w and 6 w specimens and staining. A: Achilles tendon. T: tibia. C: calcaneus. M: muscle. **C** Schematic of HE staining and magnification at 2 w and **E** 6 w. **D** The 2 w and **F** 6 w Masson staining plots, magnified images, and collagen orientation distribution based on Masson staining analysis. **G** Collagen orientation distribution scale. **P** Quantitative analysis of the collagen volume. **H** Sirius red staining at 6 w and **Q** quantitative analysis of the collagen I/III ratio. **I** CD31 immunofluorescence at 2 w and **R** quantitative analysis of the staining. **J** The 2 w and **K** 6 w SCX immunofluorescence and **S** quantitative analysis. **L** The 2 w and **M** 6 w TNMD immunofluorescence and **T** quantitative analysis. **N** The 2 w YAP immunofluorescence. **O** Schematic of stress homogenization and antiadhesion ($n = 6$, n values derived from different experimental units. The data are presented as the mean ± standard deviation. The statistical significance was determined by multiway ANOVA).

fluorescent expression of YAP at the margin of the tendon injury in the control group or the infected group, whereas significant YAP expression was detected at the margin of the tendon injury in all three treatment groups. These findings suggested that the concentrated stress at the tendon suture line could be redistributed, the stress at the end of the tendon rupture could be homogenized, and secondary rupture caused by dynamic loading could be effectively avoided. This finding was consistent with the results of mechanical testing of the hydrogel.

HAPP@H-EXO improves postoperative tissue adhesion and mechanical function

When the Achilles tendon was removed at 8 weeks after surgery, macroscopic observation revealed (Fig. 10A) that the surface of the tendon was rougher and thicker in diameter in the infection group than in the HAPP@H-EXO group, whereas there was no obvious thickening or fibrosis in the HAPP@H-EXO group, and the edges were well defined, displaying a glossy white appearance. TEM (Fig. 10B, C) revealed that the infection group presented disorganized collagen fibres and a sparsely arranged morphology, whereas the hydrogel group presented more densely ordered collagen fibres. Among them, the fibres in the HAPP@H-EXO group were larger in diameter and more regularly arranged, which was consistent with the macroscopic observations.

Postoperative ultrasonographic findings at the 8th week (Fig. 10D) revealed that the Achilles tendon border in the infection group was unclear, suggesting the presence of tissue adhesions and thickening of the tendon. After treatment with HAPP3, HAPP@EXO, or HAPP@H-EXO, the Achilles tendon was clearly separated from the surrounding tissue, with a larger hypoechoic area and smaller anterior–posterior diameters, among which the Achilles tendon in the Inf-HAPP@H-EXO group was the most clearly defined, with the smallest anterior–posterior diameter, which was closer to the normal Achilles tendon morphology (Fig. 10E, F). Tendon adhesion was further quantified by direct observation and the use of a scoring system[10,61]. The results (Fig. 10G) revealed that the infection group had the highest score, while all the treatment groups had significantly lower scores compared with the infection and control groups. The above experiments demonstrated that HAPP@H-EXO was able to prevent tissue adhesion while achieving tissue repair, confirming the utility of its Janus-mimetic asymmetric adhesion structure for antiadhesion in vivo. Moreover, compared with HAPP3, HAPP@H-EXO could prevent postoperative adhesion through antioxidative stress effects, anti-inflammatory effects, and the promotion of orderly remodelling of damaged tissues, which was consistent with the results of HE and Masson staining.

Postoperative 8-week gait analysis revealed (Fig. 10H–L) that the Inf-HAPP@EXO and Inf-HAPP@H-EXO groups relied more on heel contact, produced clearer paw prints, and presented greater contact areas and contact strengths in the hindlimbs than did the infection group. The Achilles functional index (AFI), a marker of motor function recovery after Achilles tendon injury, was calculated from the paw print parameters[62]. The results (Fig. 10M) revealed that the AFI was lowest in the infection group and highest in the Inf-HAPP@H-EXO group, indicating that HAPP@H-EXO treatment resulted in the best tissue reconstruction and functional recovery. The results of the open field test (OFT) revealed (Fig. 10N, O) that the Inf-HAPP@H-EXO group exhibited more exploratory behaviours and significant improvement in total movement distance (vs. the infection group, $p < 0.05$), which further demonstrated the facilitating effect of HAPP@H-EXO on the recovery of postoperative behavioural functions.

HAPP@H-EXO restores the mechanical properties of the Achilles tendon: A schematic diagram of the biomechanical tests is shown in Fig. 10P. The results (Fig. 10Q, R) revealed that the Inf-HAPP3, Inf-HAPP@EXO, and Inf-HAPP@H-EXO groups presented greater rupture loads and Young's moduli than did the infection group, with the Inf-HAPP@H-EXO group being the closest to the normal tendon. After HAPP@H-EXO treatment, the regenerated tendon was structurally stronger, with greater load-bearing capacity and elasticity.

In conclusion, HAPP@H-EXO not only promoted anti-infective healing of tendons but also prevented postoperative adhesion, promoted behavioural recovery, enhanced biomechanical properties, and reduced the risk of rerupture. These findings suggested that HAPP@H-EXO not only accelerated the restoration of continuity at the tissue level but also met the functional regeneration requirements of tendons and had good potential for clinical application.

HAPP@H-EXO promotes Achilles tendon healing in rabbits

To verify the clinical application potential of HAPP@H-EXO in large animals, we further evaluated its therapeutic efficacy by establishing a rabbit model of Achilles tendon rupture. Supplementary Movie 1 shows the main process of model establishment and treatment. As presented in Supplementary Fig. 19A, gross images of Achilles tendons harvested at 8 weeks revealed a rough surface, severe adhesion to surrounding tissues, and excessive tendon fibrosis in the infected group. In contrast, the Achilles tendons in the HAPP@H-EXO treatment group had smooth surfaces without obvious abnormal adhesion and were not significantly different from the normal Achilles tendons of the rabbits. Further observation and a scoring system were used to assess adhesion. The results (Supplementary Fig. 19B) revealed that the adhesion score was lowest in the HAPP@H-EXO treatment group and highest in the infected group. The adhesion score of the Interceed treatment group was also lower than that of the infected group, but its efficacy was still inferior to that of the HAPP@H-EXO treatment group. HE staining, Masson staining, and Sirius red staining at 8 weeks (Supplementary Fig. 19A, E) revealed that the collagen deposition and extracellular matrix regeneration were greater in the Inf-HAPP@EXO and Inf-HAPP@H-EXO groups than in the infected group, among which the collagen arrangement was the most regular in the Inf-HAPP@H-EXO group. In contrast, there was no significant difference between the Interceed treatment group and the infected group. The above results indicated that HAPP@H-EXO had excellent ability to prevent postoperative adhesion, whereas the Interceed treatment group did not achieve such an excellent antiadhesion effect and was also inferior to HAPP@H-EXO in promoting the orderly deposition of collagen fibres. To test the biomechanical strength after the corresponding treatments, tensile tests were performed on the harvested samples at 8 weeks. The results revealed that the failure load and Young's modulus were lowest in the infected group, whereas those in the HAPP@H-EXO group were closest to those in the normal Achilles tendon group (Supplementary Fig. 19C, D).

In conclusion, the above results fully demonstrated that HAPP@H-EXO could still promote antiadhesion and high-strength

https://doi.org/10.1038/s41467-026-68514-0

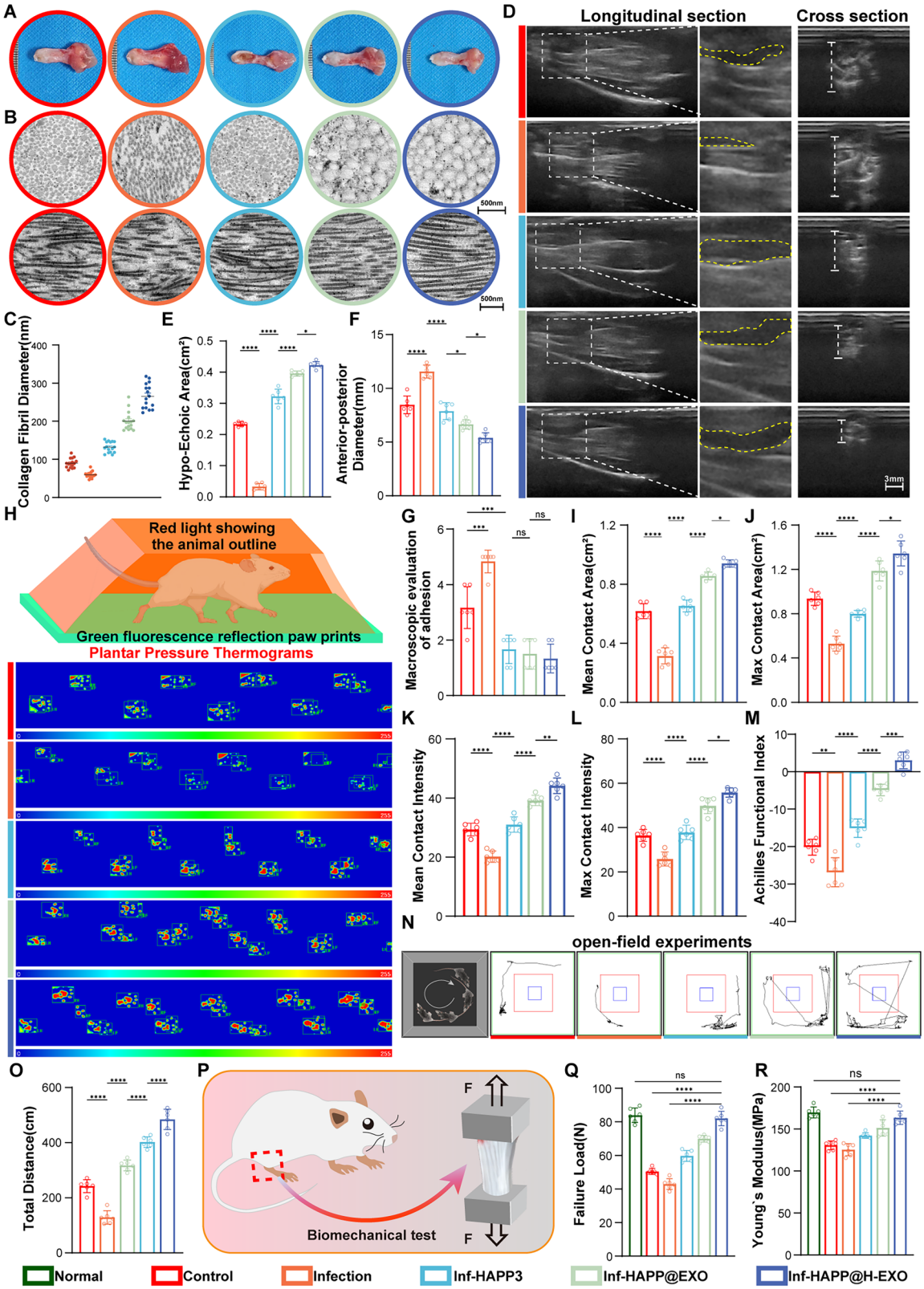

Fig. 10 | HAPP@H-EXO improves postoperative tissue adhesion, mechanical function, and mechanical properties. A Macroscopic physical image after 8 w of sampling. **B** TEM image of a tendon and **C** statistical graph of the collagen fibre diameter. **D** Ultrasound test results. **E** Quantitative hypoechoic area and **F** anteroposterior tendon diameter length. **G** Postoperative adhesion score. **H** Gait test schematic and test results. **I** Statistical graph of the mean contact area. **J** Statistical graph of the maximum contact area. **K** Statistical graph of the average contact strength. **L** Maximum contact strength statistics. **M** AFI statistics. **N** Open-field test results and **O** total distance travelled statistical graphs. **P** Schematic diagram of the biomechanical testing of the Achilles tendon. **Q** Maximum rupture load and **R** Young's modulus ($n = 3$ in the (**C**), $n = 6$ in the other statistic. n values derived from different experimental units. The data are presented as the mean ± standard deviation. The statistical significance was determined by multiway ANOVA).

healing of Achilles tendons in large animal models, which holds transformative clinical significance for the treatment of infected weight-bearing soft tissue injuries.

Discussion

The repair of ruptured and infected tendons faces multidimensional challenges, such as mechanical dysfunction, tissue adhesion, colonization by drug-resistant bacteria, and immune imbalance[1,2,11]. In this study, we designed a biomimetic Janus hydrogel that achieves structural biomimicry, spatiotemporal antimicrobial effects, and anti-inflammatory effects. Compared with existing conventional functional hydrogels[37,63–65], HAPP@H-EXO is more effective because of its four features. First, the dual-network hydrogel structure was constructed using a high-strength covalent backbone network, and a dynamic borate bonding network achieved high mechanical strength and stress redistribution. Second, an asymmetric adhesive Janus structure was constructed by utilizing the principle of polar group inmigration, which effectively addresses postoperative adhesion issues. Third, cationic antimicrobial agents and phenylboronic acid groups were loaded into the hydrogel to achieve rapid antimicrobial effects and long-lasting inhibition of drug-resistant bacteria. More importantly, exosome production and biological efficacy significantly increased after hypoxic preconditioning, and pH-responsive release occurred during the tissue repair process. This multiscale synergistic mechanism provides directions for the design of biomaterials that achieve the regeneration of load-bearing soft tissue with bacterial infection.

One of the challenges in tendon repair is restoring the unique mechanical properties of the tendon and preventing postoperative adhesions. Tendons have both high mechanical strength and anti-adhesion properties, whereas postoperative regenerated tissues often suffer from low mechanical strength and tissue adhesion, leading to immobility or even secondary rupture[16,17,50]. Li et al. developed a hydrogel with excellent mechanical properties, antifatigue properties, and the ability to achieve multiscale alignment of the fibrous structure that can adapt to the high mechanical stimulation environment in which the tendon is located and effectively promote tendon repair[66]. Liu et al. loaded bFGF/DGNs into PLLA copolymer fibres by electrostatic spinning, and the electrospun film acted as a barrier and had excellent antiadhesion effects, effectively inhibiting the adhesion between the repaired tendon and the surrounding tissues[63]. Peng et al. identified a new drug, imatinib mesylate (IM), for the prevention of tendon adhesion and loaded it into a hydrogel with ZIF-8, N-carboxyethyl chitosan (CEC), and oxidized hyaluronic acid (OHA) components to prevent peritendon adhesion through the PDGFRβ/ERK/STAT3/CLDN1 pathway[64]. These biomaterials promoted the healing process of tendons by improving their mechanical strength or preventing adhesion; however, they did not have the natural stress distribution properties of the tendon under dynamic loading, and the design of biomaterials that have antiadhesion effects can be simplified. In this study, multifunctional hydrogels with both mechanical matching and asymmetric adhesion properties were prepared. The inwards migration of polar groups on the hydrogel surface was induced by LLP, resulting in the formation of a hydrophobic interface on the soft tissue side of the peritendon and the retention of lubrication properties (5.53–6.39-fold decrease in shear force and an 89° contact angle). On the tendon side, the hydrogel was mechanically supported by the high-strength interlocking covalent structure of the PVA-NB, which strongly adhered to the tendon tissue through dynamic borate and hydrogen bonding forces. Notably, the rigid topological network constructed by covalent bonding absorbs energy through elastic deformation and converts it into potential energy, which, in combination with the low energy dissipation of the hydrogel matrix, allows the topological network to continuously store and release resilient energy[38,39]. The results of the animal model revealed that the mechanical properties of the Achilles tendons of the treated animals were similar to those of the Achilles tendons of the control animals and that postoperative adhesion was effectively prevented.

The key challenge in the repair of infected tendons is that biofilms formed by drug-resistant bacteria (e.g., MRSA) are highly resistant to antibiotics, and their secreted toxins cause extensive damage to collagen fibres, which significantly affects the tendon repair process[2,11]. Although attempts have been made to alter the tendon microenvironment using antimicrobial hydrogels, this strategy still has several shortcomings. Yang et al. designed a multifunctional PC-O@TOB capsule that could capture and eliminate bacteria while promoting healing in a rat osteomyelitis model[22]. Dicky Pranantyo et al. prepared a hydrogel with the antimicrobial cation PIM and antioxidant NAC to scavenge the drug-resistant bacteria MRSA and accelerated the healing process of infected diabetic wounds[67]. Moreover, Zhang et al. developed an adhesive and robust two-layer Janus patch with potent wet adhesion and antiadhesion properties that exerted antimicrobial effects[10]. The biomaterials in all these studies had excellent antimicrobial properties, but analyses of their ability to resist long-term infection with drug-resistant bacteria and capture bacteria are lacking. In the present study, the spatial synergistic effect of bacterial capture mediated by the phenylboronic acid moiety and membrane disruption by PEI achieved efficient, broad-spectrum, and long-lasting antibacterial and antibiofilm effects and long-lasting bacterial inhibition effects. In particular, HAPP@H-EXO not only destroys bacterial biofilms but also inhibits the adaptive evolution of drug-resistant bacteria.

During infected tendon repair, early oxidative stress damage, persistent and intense inflammation, low vascular density, and limited self-regenerative capacity often lead to prolonged healing cycles, peritendinous adhesion formation, reduced mechanical strength of the repaired tendon, and an increased risk of secondary rupture[8,18,22,23]. Li et al. prepared a tdECM hydrogel loaded with TDSC-Exos, which promoted tendon repair by promoting M2 macrophage polarization and tendon cell differentiation[55]. Dou et al. prepared an injectable chitosan hydrogel fused with human umbilical vein endothelial cell-derived exosomes (HUVEC-Exos), which effectively promoted tissue regeneration and functional recovery of injured Achilles tendons by promoting cell proliferation and regulating macrophage polarization[37]. Although these studies have reported the biological efficacy of exosomes in tendon repair, to some extent, they have neglected to investigate the regulation of the immune microenvironment under hypoxic conditions at the site of tendon injury, the loading of exosomes, or the release of exosomes in response to the injury microenvironment. In this study, hypoxic pretreatment of TDSCs increased exosome production and internalization efficiency and enhanced the effects of normal exosomes in terms of reducing oxidative stress, suppressing inflammation, and promoting vascularization and tendon regeneration (the MMP was restored by 61.77%, the IL-6 level was decreased by 34.53%, the IL-10 level was elevated by 1.44-fold, the TNMD level was increased by 2.38-fold, and the SCX level was elevated by 2.10-fold). In addition, the pH-responsive release system achieves the rapid release of exosomes to inhibit the inflammatory storm in the early stages of tissue repair and the slow release of exosomes to promote tendon regeneration in the later stages of tissue repair.

Despite the significant advances achieved by this study, several aspects still need to be investigated and discussed. First, the mechanism through which hydrogels achieve stress redistribution needs to be further analysed by in situ characterization[68]. Second, although lotus leaves are easily available and effective, they are susceptible to wilting and need to be used in a timely manner; thus, it is necessary to study their mechanism of inducing hydrophobic interfaces as well as the study and preparation of moulds that mimic the structure of lotus leaves in the future[69]. Third, the antibiotic-independent multidimensional strategy used in this study to treat

bacterial infection provides insights for combating bacterial drug resistance; however, its specific antibiofilm and antidrug resistance mechanisms requires exploration in future analyses[70]. Fourth, the microenvironmental control of exosome release kinetics should be further investigated by combining in vivo targeted tracing and dynamic pH detection in damaged microenvironments[71]. Finally, the specific functional molecules of hypoxic tendon-derived stromal cell-derived exosomes (Hypo-TDSC-Exos) were not identified in this study. Future research should combine transcriptomics and proteomics technologies to systematically identify the key active molecules[72].

In conclusion, this study reveals "structural biomimicry, spatiotemporal modulation of bacterial infection, and immunomodulation" as a strategy to promote ruptured tendon repair. HAPP@H-EXO can significantly restore Achilles tendon structure and function in rat and rabbit models of MRSA infection after Achilles tendon rupture, providing a direction for the treatment of weight-bearing soft tissue injuries in combination with bacterial infection.

Methods

Ethical statement

All animal experiments were approved by the Animal Ethics Committee of the First Affiliated Hospital of Naval Medical University (CHEC2025-017).

Experimental materials

The 5-norbornene-2,3-dicarboxylic anhydride was obtained from Shanghai Dibo Chemicals Technology Co., Ltd. Triethylamine (TEA, ≥99.5%), 4-dimethylaminopyridine (DMAP, 99%) was purchased from Shanghai Mindray Biochemical Technology Co., Ltd. Polyvinyl alcohol (PVA, type 1799) and hyaluronic acid (HA, Mw = 500–1500 kDa) was obtained from Shanghai Macklin Biochemical Co., Ltd. The 3-aminophenylboronic acid (PBA, 98%), 1-ethyl-3-(3-dimethylaminopropyl)carbodiimide hydrochloride (EDC·HCl, ≥99%), and N-hydroxysuccinimide (NHS, 98%) were obtained from Shanghai Aladdin Biochemical Technology Co., Ltd. Oligo-polyethyleneimine (PEI, 99%, Mw = 600) was purchased from Shanghai Adamas Reagent Co., Ltd. TDSCs were isolated from rat Achilles tendons. All other cells, antibodies, and culture media were purchased from Shanghai Jiajun Biotechnology Co., Ltd. All the kits, PE tubes, and other basic consumables were purchased from Shanghai Hanke Biotechnology Co., Ltd. All the chemical reagents were directly used in the material synthesis experiments without additional laboratory purification.

Synthesis of phenylboronic acid-modified hyaluronic acid (HP)

HA (1 g) was dissolved in 100 mL of phosphate buffer solution (pH = 5.5). In a HA:PBA:EDC·HCl:NHS molar ratio of 1:2:2.5:2.5, PBA, EDC·HCl, and NHS were dissolved in 40 mL of ultrapure water. The pH of the mixture was adjusted to 5.5, after which the HA solution was slowly added. The reaction system was magnetically stirred at room temperature for 24 h, followed by dialysis (MWCO 3500 Da) against ultrapure water for 4 days with water replaced at least three times daily. After dialysis, the sample was lyophilized to obtain the HP. The chemical structures of HA-PBA were analysed using a Bruker INVENIO S-Hyperion 3000 Fourier transform infrared (FT-IR) spectrometer (Germany) and a Lambda 950 UV–Vis spectrophotometer. On the basis of the results of UV–Vis absorption spectroscopy, the amount of 3-aminophenylboronic acid grafted on HA was quantified by establishing a standard curve for its characteristic absorption peak.

Synthesis of norbornene-modified polyvinyl alcohol (PVA-NB)

First, 5 g of 1799 PVA was added to 100 mL of anhydrous dimethyl sulfoxide (DMSO). The mixture was subjected to vacuum treatment for 1 h under continuous stirring, followed by purging with argon to remove air and moisture. The solution was then heated to 90 °C to ensure complete dissolution of the PVA in anhydrous DO. After cooling to room temperature, the system underwent a second vacuum treatment (1 h) and argon purging to achieve an anhydrous/oxygen-free environment. Under argon protection, 5-norbornene-2,3-dicarboxylic anhydride, triethylamine (TEA), and 4-dimethylaminopyridine (DMAP) were sequentially added to the system. The reaction proceeded at 50 °C under an argon atmosphere with magnetic stirring for 24 h. The resulting solution was transferred into dialysis tubing (molecular weight cut-off [MWCO] 3500 Da) and dialysed against ultrapure water for 2 days, followed by overnight dialysis in sodium carbonate buffer. This dialysis protocol (buffer + water) was repeated twice, with a final 5-day dialysis in ultrapure water. The product was lyophilized to obtain PVA-NB. The molecular structure of the PVA-NB was qualitatively and quantitatively analysed using an AVANCE III NMR spectrometer (^{1}H NMR).

Preparation of the hydrogels

HP and PEI were dissolved in ultrapure water to prepare a 1% (w/v) HP mixed solution, with the solid PEI content set at five gradients: 0%, 1.1%, 1.7%, 2.3% and 2.9%. PVA-NB was separately dissolved in ultrapure water to prepare a 20% (w/v) stock solution. The two solutions were mixed at a 1:1 volume ratio, followed by the addition of the photoinitiator LAP and crosslinker DTT. The mixture was homogenized using a vortex mixer for 3 min to form the hydrogel precursor. The precursor was then transferred into moulds and cross-linked via UV irradiation to obtain hydrogels, which were designated HAP, HAPP1, HAPP2, HAPP3, and HAPP4 on the basis of the PEI content. For the composite hydrogels, 2 mL of Nor-Exos precipitate and 2 mL of Hypo-Exos precipitate were separately added to 1 mL of PVA-NB storage solution, followed by mixing with 1 mL of HP solution (PEI content: 0.8%). The above preparation procedure was then repeated to obtain HAPP@EXO and HAPP@H-EXO hydrogels.

To prepare the hydrogel extract, 5 mL of hydrogel was added to a 50 mL centrifuge tube, followed by the addition of 20 mL of DMEM medium, incubation overnight, and centrifugation (3000 rpm, 5 min) and extraction of the supernatant.

Basic properties of the hydrogels

Gelation time of the hydrogels. The gelation time of hydrogels with varying solid PEI contents was measured using the vial inversion method. The detailed procedures were as follows. The 1% HP mixed solution (with different solid PEI contents) and 20% PVA-NB stock solution were mixed at a 1:1 volume ratio in centrifuge tubes. LAP photoinitiator and DTT crosslinker were added, followed by homogenization using a high-speed vortex mixer. The mixture was exposed to UV light. The transition from the flowable sol state to the fixed gel state was monitored by periodically inverting the glass vial. The UV irradiation time required for this transition was immediately recorded as the gelation time. Eight parallel tests were performed for each hydrogel group to ensure data reliability.

Water retention performance of hydrogels. Hydrogel samples of equal volume were placed under ambient conditions (25 °C, open environment). The weight of each hydrogel was recorded at 1-h intervals, and the water retention capacity was calculated using the following formula

$$WR(\%) = (W_n/W_0) \times 100\% \quad (1)$$

W_0: initial weight of the hydrogel

W_n: the weight at different time points.

For each hydrogel group, seven independent tests were conducted to ensure reproducibility.

Water supply performance of hydrogels. In an open environment at room temperature, the hydrogel samples from each group were

placed on artificial skin. The water supply capacity was calculated by measuring the real-time weight of the artificial skin at 1-h intervals using the following formula:

$$WS(\%) = (W_n - W_0)/W_0 \times 100\% \quad (2)$$

W_0: the initial weight of the artificial skin

W_n represents the weight after contact with the hydrogel for different durations.

Artificial skin was prepared from a 20% (w/v) gelatine solution. For each hydrogel group, eight independent experiments were conducted to ensure statistical robustness.

Swelling performance of hydrogels. At a constant temperature of 37 °C, equal volumes of lyophilized hydrogel samples were immersed in PBS (pH 7.4) in centrifuge tubes. At predetermined time points, the hydrogels were removed, gently blotted with filter paper to remove surface liquid, and immediately weighed until swelling equilibrium was reached. Ten independent replicates were performed for each hydrogel group.

The swelling ratio (SR) and equilibrium swelling ratio (ESR) were calculated using the following formulas:

$$SR = (W_t - W_0)/W_0 \quad (3)$$

$$ESR = (W_{eq} - W_0)/W_0 \quad (4)$$

W_t: Weight of the hydrogel after swelling for a specific time

W_0: Initial weight of the lyophilized hydrogel

W_{eq}: Weight at swelling equilibrium.

Degradation performance of hydrogels. Equal volumes of lyophilized hydrogel samples were immersed in phosphate-buffered saline (PBS, pH = 7.4) in centrifuge tubes. The tubes were placed in a constant-temperature orbital shaker (37 °C, 150 rpm) for degradation studies. Fresh PBS was replaced every 24 h to maintain a consistent degradation environment. At predetermined time points, the hydrogel samples were removed, gently rinsed with ultrapure water to eliminate residual salts, lyophilized, and precisely weighed to calculate the remaining weight percentage. Eight parallel experiments were conducted for each hydrogel group.

The degradation rate was quantified as follows:

$$\text{Remaining weight}(\%) = (W_t/W_0) \times 100\% \quad (5)$$

W_t: Lyophilized weight of the hydrogel after degradation for t days

W_0: Initial lyophilized weight of the hydrogel.

Topological morphology of hydrogels. The microscopic morphology of the hydrogels was characterized using scanning electron microscopy (SEM). The procedure was as follows. The hydrogel samples were fully swollen in deionized water until they reached mass equilibrium, after which they were lyophilized. The lyophilized samples were sputter-coated with gold to enhance surface conductivity. Coated samples were mounted on the stage of a Hitachi S-3400 N scanning electron microscope. Microstructural features were observed and recorded under optimized imaging conditions. Pore size distribution was quantified using image analysis software (e.g., ImageJ). To ensure the statistical significance of the observations, no fewer than three independent samples were selected for each hydrogel group to guarantee data reliability and representativeness.

Mechanical properties of hydrogels

Rheological properties of the hydrogels. The viscoelastic properties and structural stability of the hydrogels were evaluated using an MCR 501 rotational rheometer with the following testing protocol. Hydrogel samples were subjected to strain sweep testing at a fixed frequency of 1 Hz, with strains ranging from 0.1% to 100%. The linear viscoelastic region (LVER) was identified by analysing the dependence of the storage modulus (G′) and loss modulus (G″) on the strain amplitude. To ensure data reliability, no fewer than three replicates were tested per group. The hydrogels were continuously scanned for 600 s under dynamic oscillatory mode at constant temperatures (25 °C and 37 °C). Real-time changes in G′ and G″ were monitored to assess structural stability. A minimum of three independent tests were conducted per group to confirm reproducibility.

Tensile testing of hydrogels. The prepared hydrogel samples were cut into standard rectangular samples (30 mm × 10 mm × 5 mm) and subjected to uniaxial tensile testing using a universal testing machine. The tensile rate was set to 20 mm/min. Five parallel tests were conducted for each group to ensure data reliability. The maximum tensile strength and toughness of the hydrogels were calculated from the stress–strain curves.

Compression testing of the hydrogels. The mechanical properties of the hydrogels were evaluated using single-cycle compression tests. Cylindrical hydrogel samples (8 mm in diameter and 11.5 mm in height) were prepared and placed between parallel plates of a universal testing machine (Shanghai Hengyi HY-0230). An axial compressive load was applied at a constant rate of 40 mm/min until 80% strain was reached, at which time one compression cycle was completed. Five parallel specimens were tested per group, and stress–strain curves during compression were recorded. The compressive strength, toughness, and energy dissipation of the hydrogels were quantitatively assessed on the basis of the stress–strain curves at 80% strain.

Finite element analysis (FEA) of hydrogels

Modelling and material constitutive relation. A 3D modelling software was used to construct a structural model of the hydrogel–tendon–suture joint, and the finite element method was adopted to simulate the tensile conditions. An isotropic linear elastic constitutive model was applied to the tendon and suture, which is expressed as $\sigma = D^{el}\varepsilon^{el}$. Here, σ denotes the Cauchy stress tensor, D^{el} represents the elastic tensor, and ε^{el} represents the strain tensor. The elastic modulus of the tendon is 500 MPa, that of the hydrogel is 300 kPa, and that of the suture is 2 GPa. For the hydrogel, a time-domain linear viscoelastic model was employed, with the expression $\tau(t) = \int_0^t G^R(t\text{-}s)\dot{\gamma}(s)ds$. In this equation, $\tau(t)$ is the interfacial shear stress, G^R refers to the shear relaxation modulus (a response used for material characterization), and $\dot{\gamma}(s)$ denotes the shear strain rate.

Contact setup and damage mechanism. Two key contact interfaces were defined: 1. Tendon–suture interface: Frictionless rigid contact was used to achieve force transmission. 2. Tendon–hydrogel interface: A cohesive contact model was adopted to simulate the material interface behaviour of the hydrogel on the tendon, i.e., the adhesive effect of the hydrogel. During initial loading, the stress and displacement in the cohesive contact model exhibit a linear relationship. When the damage criteria (e.g., maximum nominal stress) are met, damage initiates, leading to gradual degradation of the interface stiffness and a decrease in load-bearing capacity. The expression of the cohesive contact is as follows: $\mathbf{t} = \begin{Bmatrix} t_n \\ t_s \\ t_t \end{Bmatrix} = \begin{bmatrix} K_{nn} & 0 & 0 \\ 0 & K_{ss} & 0 \\ 0 & 0 & K_{tt} \end{bmatrix} \begin{Bmatrix} \delta_n \\ \delta_s \\ \delta_t \end{Bmatrix} = \mathbf{K}\delta$, where t is the traction tensor, K is the stiffness matrix, and δ is the

displacement. When the maximum nominal stress is reached, the interface stiffness degrades and the load-bearing capacity decreases. In this study, an applied load of 0.1 N was used, and it was assumed that the hydrogel would not undergo damage under this force, indicating that the hydrogel maintained efficient performance throughout the process. Additionally, to avoid excessive complex contact calculations that increase the difficulty of simulation convergence, the modelling process was optimized: the suture was modelled inside the tendon adjacent to the boundary. This design eliminates the need for contact between the suture and the hydrogel, and we consider this modelling treatment to have a negligible effect on the simulation process.

Viscoelastic parameter fitting. Analysis of the constitutive equation for time-domain linear viscoelasticity revealed that the time-dependent relationship of the modulus was essential for establishing the constitutive model. Specifically, the modulus under different strain conditions could be obtained by differentiating the stress with respect to the strain; each strain condition corresponded to a specific deformation time. Thus, a curve describing the modulus as a function of time could be plotted, and the Prony series could be used to fit this time-dependent process. The dimensionless relaxation modulus is characterized by $g_R(t) = G_R(t)/G_0$, where G_0 denotes the initial modulus. The Prony series was employed to fit the time dependence of this dimensionless relaxation modulus, expressed as follows: $g_R(t) = 1 - \sum_{i=1}^{N} \bar{g}_i^p \left(1 - e^{-e/\tau_i^G}\right)$. In this equation, N, $\bar{p}_i$, and $\tau_i^G (i = 1, 2 \cdots, N)$ are material constants with specific values determined by fitting the experimental data.

Result analysis. To conduct a statistical analysis, the stress changes of the 10 meshes at the tendon edge were selected, and a time–stress curve was plotted. The loading protocol for the curve was defined as follows: a progressive load was applied to reach 0.1 N from 0 to 3 s, followed by a static hold (constant load) from 3 to 8 s. All simulations in this work were conducted using the commercially available software ABAQUS 2019 (SIMULIA, France).

Evaluation of hydrogel fatigue resistance and energy storage stability

Cyclic compression testing of the hydrogels. The fatigue resistance of the hydrogels was assessed through 100 consecutive compression cycles. Hydrogel samples were prepared as described above and surface-sealed with silicone oil to increase environmental humidity and reduce friction effects. A universal testing machine was used to apply axial compression at a rate of 40 mm/min until 80% strain was reached for 100 cycles. The fatigue resistance parameters were analysed on the basis of the stress–strain curves from each cycle. Four replicates were tested per hydrogel group.

Static compression testing of the hydrogels. The hydrogel samples were machined into cylinders (8 mm in diameter and 11.5 mm in height) following standard compression testing protocols and mounted between parallel plates of a universal testing machine. An axial load was applied at a constant rate of 40 mm/min until 80% compressive strain was achieved, after which the plate position was fixed to maintain the strain. Stress relaxation behaviour was monitored by recording real-time stress decay curves over time via a force transducer. Four replicates were tested per hydrogel group.

Static tensile testing of the hydrogels. The hydrogels were machined into standard rectangular samples (30 mm × 10 mm × 5 mm) and subjected to uniaxial tensile loading using a universal testing machine at a rate of 20 mm/min. Upon reaching 60% tensile strain, the position was fixed to maintain constant strain. Stress decay data were continuously acquired via a force transducer, synchronously recording time–stress curves. The stress relaxation behaviour under constant tensile strain was evaluated on the basis of real-time monitoring. Four replicates were tested per hydrogel group.

Self-healing, injectable, and adaptive properties of hydrogels

Self-healing properties of hydrogels. Hydrogel disc samples were dyed and longitudinally bisected along the central axis to obtain semicircular cross-sections. Semicircular slices of different colours were closely aligned and bonded. After the self-healing process, the repaired hydrogel discs underwent tensile mechanical testing to evaluate their self-healing performance.

The self-healing properties of the hydrogels were quantitatively assessed through uniaxial tensile testing. Rectangular hydrogel samples (30 mm × 10 mm × 2 mm) were prepared according to tensile testing standards. A transverse symmetric incision (penetrating the entire thickness) was made at the sample midpoint using a scalpel. The cut surfaces were aligned, gently pressed for contact, and incubated in a warm and humid environment (25 °C, 90% RH) for 24 h to allow self-repair. Posthealing, the samples were mounted on a universal testing machine (Instron 5966) and subjected to uniaxial tensile testing at 20 mm/min. Stress–strain curves were recorded to calculate the tensile strength of the healed hydrogels. Three replicates per group were tested.

The self-healing efficiency (SHE) was determined as follows:

$$\text{self} - \text{healing efficiency}(\%) = (\sigma_{\text{self}-\text{healing}}/\sigma_{\text{original}}) \times 100\% \quad (6)$$

$\sigma_{\text{self-healing}}$: Tensile fracture stress of healed hydrogels
σ_{original}: Tensile fracture stress of pristine hydrogels

Injectable and adaptive performance of hydrogels. The hydrogel precursor solution was loaded into a syringe, and its injectability was evaluated by observing whether it could be uniformly extruded through the needle orifice. The solution was subsequently injected into a defect site in the pig liver and photo-cross-linked under UV irradiation to form a gel. The spatial adaptability and wet adhesion properties of the resulting hydrogels were subsequently assessed.

Wet adhesion properties of hydrogels

Lap shear tensile testing. Fresh pig skin was pretreated by cutting rectangular specimens (9 cm × 2 cm) and soaking them in PBS for 1 h. The hydrogel precursor solution was uniformly coated onto two pig skin surfaces, which were then aligned and bonded under UV irradiation at room temperature to form a hydrogel interlayer with an effective adhesion area of 2 × 1 cm^2. Shear tensile testing was performed using a universal testing machine (Shanghai Hengyi HY-0230) at a rate of 10 mm/min. The fracture load was recorded to evaluate hydrogel adhesion to pig skin tissue. No fewer than three replicates were tested per group.

Burst pressure testing. A real-time burst pressure monitoring system was established. After the skin and small intestinal tissue of the pigs were cleaned, full-thickness circular defects (2 mm diameter) were created using a biopsy punch. The hydrogel precursor was applied to moist defect surfaces and UV-cured at room temperature. PBS was continuously infused into the system at a constant flow rate of 2 $mL \cdot min^{-1}$ while pressure changes were monitored. The critical pressure at hydrogel seal failure (indicated by leakage) was recorded as the key metric for assessing tissue adhesion and sealing ability. A minimum of three replicates were tested per hydrogel group to ensure reliability.

Construction and validation of asymmetric adhesion janus hydrogels

Mould construction. First, freshly harvested lotus leaves and custom-made polyethylene (PE) moulds were washed with water, followed by sterilization treatment under ultraviolet (UV) irradiation. Fresh and sterile lotus leaf pieces of appropriate size were subsequently cut, smoothly attached to the inner wall of the PE tube, and fixed using medical-grade cyanoacrylate bioadhesive. This mould served only as a temporary shaping tool and was removed after hydrogel injection and UV curing; it did not form any chemical bonds with the hydrogel throughout the entire process.

Tissue adhesion test. An isolated rat Achilles tendon was infiltrated with PBS for 1 h, after which the outer layer was covered with LLP, and an appropriate amount of hydrogel precursor was injected into the gap between the LLP and the tendon. The LLP was removed after 5 min of light curing, and the hydrogel was wrapped with a layer of PBS-infiltrated pigskin for 1 h. In the WR group, the hydrogel precursor was injected directly between the skin and the tendon and then cured by photocrosslinking. Displacement–adhesion curves at the skin–hydrogel interface were recorded by pulling the Achilles tendon and the skin at a tensile rate of 10 mm/min on a universal testing machine (Shanghai Hengyi HY-0230). To ensure that the Achilles tendon–hydrogel adhesion area was the same as the pigskin–hydrogel adhesion area, the Achilles tendon was considered a cylinder, and the contact area of the Achilles tendon–hydrogel was obtained by calculating the radius of its cross-section (r_1) and the length of the hydrogel adhesion (L_1) ($S_1 = 2\pi r_1 L_1$). For the composite cylinder (radius $r_2 > r_1$) formed by wrapping the pigskin around the outer layer of the hydrogel, the required wrapping length was back-calculated by the derivation of the formula ($L_2 = r_1 L_1 / r_2$) so that the hydrogel–pigskin contact area ($S_2 = 2\pi r_2 L_2$) was strictly equivalent to that of S_1. The test was repeated 3 times.

Contact angle test. Water was dripped from a needle onto the surface of a freeze-dried HAPP3 hydrogel sample, and the contact angle between the droplet and the sample surface was recorded in real time with the help of a contact angle measuring instrument (SGC-QH33) with the function of automatic continuous recording. The test was repeated 4 times.

Energy dispersive X-ray spectroscopy analysis. Scanning electron microscopy (SEM) was used to observe the dried hydrogel samples subjected to different treatments. Additionally, energy dispersive X-ray spectroscopy (EDS) was employed to visually analyse the elements on the hydrogel surface to track the arrangement of the polar groups on the polymer chains.

Cell adhesion test. The hydrogel precursor was placed in six-well plates, treated with LLP, and cured under UV light to form a gel. L929 cells (3×10^6 cells/well) were cultured in six-well plates with a hydrogel substrate, while the control group did not contain a hydrogel substrate. After 12 h, the supernatant was discarded, digested with trypsin, divided into six portions and placed in 96-well plates, after which the OD value was measured using an enzyme marker at 450 nm to calculate the cell adhesion rate. Moreover, the morphology of L929 cells was visualized by phalloidin staining, and the expression of F-actin, FN, COL 1A1, and MMP was detected by Western blotting. The outlines of the cells in the fluorescence images were manually traced using ImageJ, and the total cell area and perimeter were measured. The total spread area and perimeter were subsequently divided by the number of cells to obtain the average spread area and perimeter of each cell. The cell adhesion rate (CAR) was calculated according to the following formula:

$$CAR(\%) = (OD_e - OD_b / OD_c - OD_b) \times 100\% \quad (7)$$

ODe: the absorbance value of the supernatant of the experimental group

ODc: the absorbance value of the control group supernatant

ODb: the absorbance value of the supernatant of the blank group

The group design was as follows:

OAR group (outer-surface antiadhesive remoulding). After the hydrogel was injected into a six-well plate, the surface was covered with a circular LLP mould. After 1 minute of UV irradiation, the sample was demoulded to obtain a hydrogel with a smooth surface.

WR group (without remoulding). Only the hydrogel was injected, and then, UV irradiation was performed without the use of a mould for treatment.

Control group. The cells were cultured in a normal six-well plate without any hydrogel treatment.

Blank group. There was only culture medium in the six-well plate without cells.

Evaluation of the bacterial capture capacity of hydrogels

Bacterial capture kinetics. The target bacterial strains were inoculated in LB liquid medium and cultured in a 37 °C shaker until they reached the logarithmic growth phase. The bacterial cells were enriched via centrifugation, washed three times with physiological saline to remove residual medium, and resuspended in saline to obtain a bacterial suspension of 10^6 CFU/mL. A 1 mL aliquot of the suspension was coincubated with 300 mg of hydrogel at 37 °C under static conditions. The supernatants were collected at predetermined time points, and the bacterial concentration was determined by measuring the optical density (OD) at 595 nm using a microplate reader. A blank control (a bacterial suspension without a hydrogel) was processed identically. Four parallel samples were tested per group to ensure data reliability. The bacterial capture ratio (BCR) was calculated as follows:

$$BCR(\%) = \left(1 - \frac{OD_n}{OD_0}\right) \times 100\% \quad (8)$$

OD_0: OD value of the blank control supernatant

OD_n: OD value of the hydrogel-treated supernatant

Assessment of bacterial capture capacity. Hydrogels and bacterial suspensions (10^6 CFU/mL) were prepared as described. Hydrogel samples were coincubated with 1 mL of bacterial suspension at 37 °C for 1 h. After incubation, the supernatants were collected, and the changes in bacterial concentration were evaluated via OD measurements at 595 nm. Blank controls (hydrogel-free bacterial suspensions) were processed in parallel. Four replicates were tested per group.

Bacterial resistance to capture testing. After the bacterial capture experiments were performed, the supernatants containing uncaptured bacteria were transferred to centrifuge tubes. Bacterial cells were collected via centrifugation and washed five times with physiological saline to remove residual hydrogel. The washed cells were transferred to LB liquid medium and cultured at 37 °C until they reached the logarithmic phase. Bacterial suspensions (10^6 CFU/mL) were reprepared, and the capture assay (including cell collection, washing, and suspension preparation) was repeated for 14 cycles. The capture ratios of pristine and 14th-passage bacterial suspensions were compared to assess bacterial resistance to hydrogel capture. Four parallel samples were tested per group.

Antibacterial properties of hydrogels

Bactericidal kinetics of the hydrogels. The hydrogel samples were sterilized in a UV sterilization chamber for 24 h prior to use. *Staphylococcus aureus*, *Escherichia coli*, and methicillin-resistant *Staphylococcus aureus* (MRSA) were separately inoculated in LB liquid medium and cultured at 37 °C with shaking until they reached a bacterial concentration of 10^9 CFU/mL. A 1 mL aliquot of bacterial suspension was coincubated with 300 mg of hydrogel at 37 °C and 150 rpm. The OD_{595} value of the suspension was measured at predetermined time points, and the antibacterial ratio (AR) was calculated as follows:

$$AR(\%) = (1 - OD_h/OD_1) \times 100\% \quad (9)$$

OD_h: OD_{595} value of the hydrogel-treated bacterial suspension
OD_l: OD_{595} value of the blank control (hydrogel-free bacterial suspension)

Four replicates were tested per group under identical conditions.

Antibacterial capacity assessment via plate spreading. Sterile hydrogels and bacterial suspensions (*S. aureus*, *E. coli*, and MRSA, 10^9 CFU/mL) were prepared as described. A 1 mL aliquot of bacterial suspension was coincubated with 300 mg of hydrogel for 6 h (37 °C, 150 rpm). Subsequently, 50 µL of the serially diluted bacterial suspension was spread evenly on freshly prepared LB agar plates and incubated at 37 °C. Colonies were photographed and counted once they reached a suitable size. A blank control (hydrogel-free bacterial suspension) was processed identically. At least three replicates were tested per group. The antibacterial ratio (AR) was calculated as follows:

$$AR(\%) = (1 - M_h/M_1) \times 100\% \quad (10)$$

M_h: Colony count on agar plates from hydrogel-treated groups
M_l: Colony count on agar plates from the blank control group

Morphological evaluation of bacteria after coincubation with hydrogels. For direct visualization of bacterial morphology, hydrogel-coincubated bacterial samples were transferred to 4 °C and fixed with 2.5% (v/v) glutaraldehyde for 3 h to stabilize cellular structures. Fixed samples were dehydrated using a graded ethanol series (30%, 50%, 70%, 90%, and 100% v/v), with each concentration applied for 15 min to gradually replace the intracellular water. The dehydrated samples were observed using field-emission scanning electron microscopy (FE-SEM, JSM-IT800) to analyse surface structural and morphological changes.

Bacterial resistance testing. Sterile hydrogels and bacterial suspensions (10^9 CFU/mL) were prepared as described previously[1]. A 300 mg hydrogel sample was mixed with 1 mL of bacterial suspension and incubated at 37 °C and 150 rpm for 12 h. After incubation, the OD_{595} of the supernatant was measured to calculate the antibacterial ratio (AR). A blank control (hydrogel-free bacterial suspension) was processed in parallel, with four replicates per group. The bacterial cells were collected via centrifugation, washed five times with sterile PBS to remove residual hydrogel, and transferred to 2 mL of fresh LB medium for regrowth to 10^9 CFU/mL. This incubation-wash-regrowth cycle was repeated for 14 passages. The AR values for pristine and 14th-passage bacteria were compared to assess resistance development.

Long-term antibacterial performance testing. Hydrogels and bacterial suspensions (10^9 CFU/mL) were prepared as described. A 300 mg hydrogel sample was mixed with 1 mL of bacterial suspension and incubated at 37 °C and 150 rpm, after which real-time OD_{595} monitoring was performed. A blank control was processed identically. At least three replicates per group were tested. Long-term antibacterial performance was evaluated using the following equation:

$$AR(\%) = (1 - OD_h/OD_1) \times 100\% \quad (11)$$

OD_h: OD_{595} value of the hydrogel-treated suspension
OD_1: OD_{595} value of the blank control.

Reusability of bactericidal efficacy. Hydrogels were mixed with *S. aureus*, *E. coli*, or MRSA suspensions (1×10^9 CFU/mL) at a ratio of 300 mg of hydrogel to 1 mL of suspension and incubated at 37 °C and 150 rpm for 6 h. After incubation, 100 µL of the mixture was collected for OD_{595} measurement. The hydrogel was gently rinsed three times with sterile PBS to remove adherent bacteria and reused in fresh bacterial suspension (1 mL, 1×10^9 CFU/mL) for three consecutive cycles. No fewer than three parallel samples were tested per experimental cycle. The reusability and bactericidal efficacy of the hydrogels were evaluated by comparing the antibacterial ratios across different cycles.

Anti-biofilm performance testing of hydrogels

The hydrogel samples were prepared as previously described. Bacterial suspensions (10^9 CFU/mL) were inoculated into 24-well plates and incubated at 37 °C for 48 h to form mature biofilms. After the culture medium was removed, the biofilms were gently washed three times with PBS to remove planktonic bacteria. The hydrogels were applied to the biofilms, followed by three additional PBS washes posttreatment. Biofilms were stained with crystal violet for 30 min, washed to remove unbound dye, air-dried, and photographed. Stained biofilms were dissolved in 95% ethanol, and the absorbance at 562 nm was measured using a microplate reader. Four replicates were tested per group. Biofilm disruption (BD) was calculated as follows:

$$BD(\%) = (1 - OD_h/ODc) \times 100\% \quad (12)$$

OD_h: Absorbance of the hydrogel-treated groups;
OD_c: Absorbance of the blank control groups.

Biocompatibility testing of the hydrogels

Cytocompatibility: extraction of lotus leaf extract. First, 10 g of fresh lotus leaves was removed, sterilized, cut into pieces and placed in a juicer. After addition of 100 mL of pure water, the sample was stirred for 5 min, and then the mixture was filtered. The filtered liquid was centrifuged at 1500 rpm for 5 min, and the resulting liquid was the lotus leaf extract.

L929 cells were seeded into 96-well plates (2000 cells/well) and cocultured with hydrogel extracts or lotus leaf extract (100 µL per well). After 12, 24, and 48 h, the cells were stained with Live/Dead reagent (AM:PI:Buffer = 1 µL:1 µL:1 mL) for 20 min, washed three times with PBS, and imaged using a fluorescence microscope (Leica, Germany) to analyse their viability. The test was repeated 6 times.

Hemocompatibility. Rat arterial blood was collected into anticoagulant-treated tubes. Lyophilized hydrogel samples (10 mg) were swollen in PBS to equilibrium. Blood was centrifuged (1500 rpm, 10 min) to separate the plasma and erythrocytes. Erythrocytes were washed three times with PBS and resuspended as a 4% (v/v) suspension. A 1 mL aliquot was coincubated with swollen hydrogel at 37 °C and 150 rpm for 2 h. Controls included the following: positive control: erythrocytes treated with ultrapure water; negative control: erythrocytes treated with PBS.

After incubation, the mixtures were centrifuged (1500 rpm, 10 min), and 100 µL of the supernatant was transferred to a 96-well plate for OD_{540} measurement. The haemolysis ratio (HR) was

calculated as follows:

$$HR(\%) = (OD_{sample} - OD_{negative})/(OD_{positive} - OD_{negative}) \times 100\% \quad (13)$$

OD_{sample}: Absorbance of the hydrogel-treated groups;
$OD_{negative}$: Absorbance of the PBS-treated control;
$OD_{positive}$: Absorbance of the ultrapure water-treated control.
Four replicates were tested per group.

In vivo host response. Nine female *SD* rats were randomly selected. The HAPP3 hydrogel was subcutaneously injected into the dorsal region using a 1 mL syringe. At 3 months, three rats were euthanized under anaesthesia. The heart, liver, spleen, lungs, and kidneys were harvested, paraffin-embedded, sectioned, and H&E-stained to evaluate tissue responses.

In vivo degradation of the hydrogels was subsequently performed. Fluorescent Labelling: The hydrogel was labelled with DiR fluorescent dye using the physical blending method at a specific concentration of 5 μM. This dye exhibits excellent lipophilicity and can be stably embedded in the hydrophobic microdomains of the hydrogel.

Six- to eight-week-old C57BL/6 mice ($n = 6$) were anaesthetized by isoflurane inhalation. Under aseptic conditions, the skin overlying the Achilles tendon was exposed, and a longitudinal incision (~5 mm) was created. Two millilitres (2 mL) of HAPP3 hydrogel precursor solution was injected into the tissue interstitium around the Achilles tendon to cover the surgical site. Following UV light cross-linking, the skin incision was closed with interrupted 6-0 absorbable sutures. Postoperatively, fluorescence imaging of the injection site was performed every 7 days using an IVIS Lumina live imaging system to monitor hydrogel retention in vivo, with tracking continuing until complete degradation.

Isolation, culture and characterization of TDSCs

Isolation and culture of TDSCs. Under aseptic conditions, Achilles tendon tissues were isolated from 6-week-old Sprague–Dawley (SD) rats. Surrounding adipose tissue, blood vessels, and tendon sheaths were meticulously removed. The tissues were rinsed three times with PBS (containing 1% penicillin–streptomycin) and minced into 1–2 mm^3 fragments. Subsequently, 5 mL of 0.1% type I collagenase solution was added, and the mixture was digested in a 37 °C thermostatic shaker (150 rpm) for 1 h. The digested suspension was filtered through a 70 μm cell strainer to remove debris, followed by three cycles of centrifugation and resuspension in PBS. The resulting cell pellets were cultured in α-MEM supplemented with 5% foetal bovine serum (FBS) and 1% penicillin–streptomycin under hypoxic conditions (5% CO_2, 1% O_2, 37 °C) in a humidified incubator.

Characterization of TDSCs. The isolated cells were identified by flow cytometry. Third-passage TDSCs (70–90% confluency) were digested with 0.25% trypsin for 2 min, followed by neutralization using culture medium supplemented with 10% foetal bovine serum (FBS). The cells were subsequently centrifuged (200 × *g*, 5 min) and resuspended in PBS to adjust the cell density to 1×10^6 cells/mL. The suspension was filtered through a 35 μm cell strainer to remove aggregates. Aliquots of 100 μL of cell suspension (1×10^5 cells per tube) were incubated with antibodies against the positive markers CD90 and CD44 in the dark for 30 min prior to flow cytometric analysis. The test was repeated 3 times.

Isolation and characterization of exosomes

Isolation and preservation of exosomes. When the third passage of the TDSCs reached 70–90% confluence, the culture medium was replaced with α-MEM supplemented with 10% exosome-depleted FBS. After 48 h of culture, the supernatant was collected and centrifuged at 300 × *g* for 10 min at 4 °C to remove floating cells, followed by centrifugation at 10,000 × *g* for 30 min to eliminate cellular debris. The clarified supernatant was filtered through a 0.22 μm PES membrane and transferred to ultracentrifugation tubes. The samples were ultracentrifuged at 100,000 × *g* for 60 min at 4 °C (Beckman Coulter, Shanghai, China), after which the supernatant was discarded, and the pellet was resuspended in 10 mL of PBS. This ultracentrifugation step (100,000 × *g*, 60 min) was repeated, and the final pellet was resuspended in 1 mL of PBS. Aliquots (100 μL) were stored at −80 °C.

Identification of exosomes: NTA and TEM. Exosome concentration and size distribution were analysed using nanoparticle tracking analysis (NTA), while their morphological characteristics were captured via transmission electron microscopy (TEM). The test was repeated 3 times.

Western blotting. Exosomes were lysed on ice with RIPA lysis buffer. The extracted proteins were separated by SDS–PAGE and transferred to PVDF membranes using a wet transfer method. The membranes were blocked with 5% non-fat milk, followed by incubation with primary antibodies against CD81, CD63, Alix, and calnexin at 4 °C overnight. After the samples were washed, secondary antibodies were applied, and the samples were incubated at room temperature for 1 h. The protein bands were visualized using an enhanced chemiluminescence (ECL) substrate. The test was repeated 3 times.

Usage and storage of exosomes. Exosome sustained-release experiment: Hypo-Exos were used without any dilution. They were loaded into HAPP3 hydrogels according to the aforementioned HAPP@H-EXO preparation method before the experiments were conducted.

Exosome uptake experiment: Both types of exosomes were diluted with PBS to a concentration of 1×10^9 particles/mL and then used directly.

All other cell experiments and animal experiments: Both types of exosomes were first diluted with PBS to a concentration of 1×10^9 particles/mL. HAPP@EXO and HAPP@H-EXO were subsequently prepared in accordance with the aforementioned preparation methods for use in the experiments.

Exosome uptake

Five hundred microlitres of the TDSC-Exo suspension and the Hypo-TDSC-Exo suspension were separately stained with 1 μL of Wistracker II, followed by incubation at 37 °C in the dark for 60 min to prepare fluorescently labelled exosomes. A 12-well plate preloaded with cell climbing slices was used. Each well was filled with 1 mL of TDSC (10,000 cells/mL). After the cells adhered, the two groups of fluorescently labelled exosomes were added separately and incubated overnight in a humidified incubator. Cells were fixed with 4% paraformaldehyde, permeabilized with Triton X-100, and stained with phalloidin to visualize the cytoskeleton. After they were mounted, the samples were observed and imaged using a fluorescence microscope (Leica, Germany). The fluorescence intensity was quantified using ImageJ. The test was repeated 3 times.

Exosome loading and slow release

Encapsulation of exosomes in hydrogels. An appropriate volume of exosome suspension was thoroughly mixed with Wistracker II staining solution. The mixture was subsequently washed via centrifugation (100,000 × *g*, 20 min) using PBS and ultracentrifugation. The hydrogel was then prepared following the HAPP@H-EXO protocol. After gelation, the hydrogel was imaged using fluorescence microscopy. The lyophilized hydrogel was subsequently observed via FE-TEM.

Sustained release of exosomes. The sustained release of exosomes was quantified using an ExoELISA according to the manufacturer's instructions. Briefly, 2 mL of Hypo-Exos was ultracentrifuged, and the supernatant was discarded. The exosome pellet was loaded into 2 mL

of HAPP3 hydrogel as described above. The exosome-loaded hydrogel was continuously immersed in 5 mL of PBS at a pH of 5 and 7.4. Equal volumes of supernatant were collected at designated intervals for exosome concentration analysis. The standard curve and cumulative release profile were quantified and plotted using a microplate reader. The test was repeated 3 times.

CCK-8-based cell viability analysis

TDSC and L929 cells were seeded in a 96-well plate at 2000 cells per well and incubated at 37 °C under 5% CO_2. Cell viability was assessed at 24 h, 48 h, and 72 h using a CCK-8 assay. Briefly, the original culture medium was removed, and 90 µL of fresh medium containing 10 µL of CCK-8 reagent was added to each well. After 2 h of incubation, the absorbance was measured at a wavelength of 450 nm using a microplate reader. (14) The cell survival rate (%) was calculated as follows: $(OD_{experimental\ group} - OD_{blank\ group})/(OD_{control\ group} - OD_{blank\ group}) \times 100\%$. ($n = 6$).

Scratch test. L929 and TDSC suspensions were added to 6-well plates (1 mL per well at 1×10^5 cells/mL). When the cells reached approximately 80% confluency, a straight scratch was created in the centre of each well using a 1 mL pipette tip, followed by washing with PBS. Cell migration was observed and photographed under a microscope at 0 h, 24 h, and 48 h. Migration rates were analysed using ImageJ ($n = 6$).

Tube formation assay (in vitro angiogenesis)

A 200 µL pipette, 200 µL tips, and a 48-well plate were precooled. Next, 20 µL of ABW Gold Matrigel was added to each well of the 48-well plate. The Matrigel was allowed to spread evenly at 4 °C, followed by transfer of the plate to a 37 °C incubator for solidification. HUVECs were digested and resuspended at 1×10^5 cells/mL, after which they were added to the Matrigel-coated wells. After 6 h, staining was performed using AM staining solution, and images were captured via fluorescence microscopy. The total branch length and node number were quantified using ImageJ ($n = 6$).

Immunofluorescence assay of RAW264.7 cells

RAW264.7 cells at a density of 1×10^5 cells/mL were seeded in 12-well plates preloaded with glass coverslips (1 mL per well). M1 polarization was induced by LPS treatment (1 µg/mL, 24 h). The cells were then cocultured with HAPP3, HAPP@EXO, or HAPP@H-EXO extracts for 48 h. After incubation, the cells were fixed with 4% paraformaldehyde, permeabilized with Triton X-100, and incubated with primary antibodies against iNOS and CD206 at 4 °C overnight. Following secondary antibody incubation (1 h at room temperature), the coverslips were mounted with antifade reagent. The fluorescence signals were visualized under a fluorescence microscope, and the fluorescence intensity was quantified using ImageJ ($n = 6$).

Enzyme-linked immunosorbent assay (ELISA)

Following the same induction and intervention protocols as described in the aforementioned RAW264.7 immunofluorescence assay, the supernatants from the cocultures at 6 h, 12 h, and 24 h were collected. The concentrations of IL-6 and IL-10 were measured using ELISA kits according to the manufacturer's instructions ($n = 6$).

ROS and mitochondrial membrane potential detection

TDSC suspensions at a concentration of 20,000 cells/mL were prepared and added to 12-well plates (1 mL per well). Cells were treated with 5 µL of H_2O_2 (1000 mg/mL) for 6 h to induce oxidative stress. HAPP3, HAPP@EXO, and HAPP@H-EXO extracts were subsequently added separately and incubated for 8 h. Cells were stained with DCFH-DA and JC-1, followed by observation under a fluorescence microscope. The fluorescence intensity was quantified using ImageJ ($n = 6$).

RNA sequencing of RAW264.7 cells

Total RNA was extracted from macrophages in the LPS group and LPS + HAPP@H-EXOS group using an RNA extraction kit. All the genomic profiling was performed by Gidioo Biotechnology Co., Ltd. (Guangzhou, China). Data processing, including correlation analysis, differentially expressed gene (DEG) screening, Kyoto Encyclopaedia of Genes and Genomes (KEGG) enrichment analysis, and Gene Ontology (GO) enrichment analysis, was conducted on the Omicsmart cloud platform (https://www.omics mart.com/home.html/) ($n = 3$).

WB verification of signalling pathway proteins. Cells were extracted from the LPS group and the LPS + HAPP@H-EXO group, and the expression of P65, p-P65, p-IκB-α, and IκB-α was detected via WB.

Establishment and efficacy evaluation of a postoperative MRSA infection model in rats with Achilles tendon rupture

Animal model. Healthy adult Sprague-Dawley (SD) rats (250–300 g, Shanghai Bikai Biotechnology Co., Ltd.) were anaesthetized via intraperitoneal injection of 1 mL of 1% pentobarbital sodium solution. The Achilles tendon region was shaved, disinfected with iodophor, and covered with a sterile surgical drape. A 1.0 cm longitudinal incision was created along the tendon axis, followed by blunt dissection of subcutaneous tissue to expose the entire Achilles tendon. The tendon was isolated from surrounding tissues and completely transected at its midpoint. A Kessler suture technique was applied for tendon repair, and 10 µL of MRSA suspension (1×10^7 CFU/mL) was evenly instilled into the suture gap. After 2 h of infection, the LLP was applied to the outside of the tendon. On the basis of the experimental groups, 2 mL of HAPP, 2 mL of HAPP@EXO, or 2 mL of HAPP@H-EXO precursor solution was injected into the lumen between the LLP and the tendon and cross-linked to form a gel by UV irradiation. After 5 min, the mould was removed, and the skin was sutured. The rats were returned to their cages and maintained under standard conditions. Six rats per sampling time point were used for each of the five groups.

Anti-infection analysis. On days 3 and 7, the wound tissue samples were homogenized and diluted in 10 mL of LB liquid medium. Afterwards, 100 µL of the diluted suspension was spread onto LB agar plates and incubated at 37 °C. Colonies on the agar plates were counted, and the antibacterial rate was calculated ($n = 6$).

Histological analysis. Rats were anaesthetized and killed at 2 and 6 weeks after surgery, and the tendon specimens were removed, fixed in 4% paraformaldehyde, embedded in paraffin, and sectioned longitudinally. Two-week-old samples were subjected to H&E, Masson staining, immunofluorescence costaining (CD206/CD86), immunofluorescence single labelling (TNF-α, TGF-β, CD31, TNMD, YAP, ROS and SCX), and TEM (to visualize mitochondria). Six-week-old samples were subjected to H&E staining, Masson staining, and α-SMA, TNMD and SCX staining for immunofluorescence ($n = 6$).

Macro- and electron microscopy and ultrasonic analysis. At 8 weeks post-surgery, the subcutaneous tissues of the rats were evaluated via Doppler ultrasound. The rats were anaesthetized by continuous isoflurane inhalation, shaved, and coated with ultrasound gel. The probe was slowly moved along the longitudinal axis of the Achilles tendon to acquire full-length images. The probe was then rotated 90° to capture transverse cross-sectional images. Hypoechoic areas (longitudinal view) and anteroposterior diameters (transverse view) were measured using ImageJ. Subsequently, the rats were euthanized, and the Achilles tendons were harvested for macroscopic evaluation of size, texture, and surface gloss. Tissue samples (1–2 mm^3) were collected for scanning electron microscopy (SEM) to observe collagen fibre alignment. Fibre diameters were quantified using ImageJ ($n = 6$).

Postoperative adhesion grade score. Six independent observers evaluated the degree of tissue adhesion on the basis of subcutaneous ultrasound findings, Achilles tendon size, texture, and surface gloss. Adhesion severity was scored on a 5-point scale: 1. No adhesion (no postoperative adhesions). 2. Minimal adhesion (rare adhesions). 3. Mild adhesion (limited adhesion). 4. Moderate adhesion (partial adhesion). 5. Severe adhesion (extensive adhesions). All samples were independently scored by the six observers simultaneously, with group allocation blinded during evaluation.

Biomechanical testing. At 8 weeks post-surgery, the rats were euthanized, and the Achilles tendons were harvested. The tendon cross-section was approximated as an ellipse. The major and minor axes of the cross-section were measured using Vernier callipers, and the cross-sectional area was calculated. A universal testing machine was used to apply continuous tensile loading at a constant rate of 20 mm/s until the tendons ruptured. The ultimate tensile load and elongation at break were recorded. Young's modulus was calculated on the basis of the ultimate tensile load, cross-sectional area, and elongation ($n = 6$).

Behavioural assessment. At 8 weeks post-surgery, the spontaneous locomotor behaviour of the *SD* rats was evaluated using a pressure-sensing gait analysis system. The experiments were conducted under a controlled environment (temperature: 25 ± 1 °C; humidity: 50 ± 5%). Rats freely explored a standardized runway platform while dynamic plantar biomechanical parameters—including plantar contact intensity and paw print area—were synchronously recorded ($n = 6$).

Spontaneous locomotor activity in postoperative *SD* rats was assessed using an open field test. The experiments were performed in an acoustically isolated, light-controlled laboratory. The open field apparatus consisted of a black-bottomed polycarbonate chamber (base dimensions: 50 cm × 50 cm). Individual rats were randomly placed in the chamber, and their free exploration behaviour was continuously recorded for 5 min using an overhead camera (60 fps frame rate). The total travel distance per rat was calculated ($n = 6$).

Establishment and efficacy evaluation of a postoperative MRSA infection model in rabbits with Achilles tendon rupture

Animal model. Healthy adult New Zealand rabbits (2000–2500 g; Shanghai Shengwang Laboratory Animal Breeding Co., Ltd.) were anaesthetized by early marginal vein injection of 5 mL of 1% sodium pentobarbital solution. The Achilles tendon area was incised, disinfected with povidone-iodine, and covered with a sterile surgical drape. A 2.0 cm longitudinal incision was created along the tendon axis, followed by blunt dissection of the subcutaneous tissue to expose the entire Achilles tendon. The tendon was separated from the surrounding tissue and transected at its midpoint. Tendon repair was performed using the Kessler suture technique, and 20 µL of methicillin-resistant *Staphylococcus aureus* (MRSA) suspension (1×10^7 CFU/mL) was injected evenly into the suture gap. After sufficient infection, the LLP was applied to the lateral side of the tendon. In accordance with the experimental groups, 3 mL of HAPP, 3 mL of HAPP@EXO, or 3 mL of HAPP@H-EXO precursor solution was injected into the cavity between the LLP and the tendon and cross-linked to form a gel by ultraviolet (UV) irradiation. The mould was removed after 5 min, and the skin was sutured. For the Interceed treatment group, Interceed was applied as per the standard procedure (Interceed was purchased from Shanghai Jiajun Biotechnology Co., Ltd.). The rabbits were then returned to their cages and maintained under standard conditions. At each time point, 6 Achilles tendons were sampled from each group.

Group design. Normal group: Normal Achilles tendons without any surgery or treatment.

In the control group, only the Achilles tendons were transected and then sutured.

Infected group: An infection model was established by adding methicillin-resistant *Staphylococcus aureus* (MRSA) to the sutured Achilles tendons.

Inf-Interceed group: The infected group treated with Interceed (on the basis of the infected group).

Inf-HAPP group: The infected group treated with HAPP3 (on the basis of the infected group).

Inf-HAPP@EXO group: The infected group treated with HAPP@EXO (on the basis of the infected group).

Inf-HAPP@H-EXO group: The infected group treated with HAPP@H-EXO (on the basis of the infected group).

Histological analysis. Rabbits were anaesthetized and euthanized at 8 weeks post-surgery. Tendon tissue samples were subsequently harvested, fixed in 4% paraformaldehyde, embedded in paraffin and cut into longitudinal sections. The samples were subjected to haematoxylin–eosin (H&E), Masson, and Sirius red staining. The ratio of type I to type III collagen fibres was calculated on the basis of the results of Sirius red staining ($n = 6$).

Postoperative adhesion grading score. Six independent observers evaluated the degree of tissue adhesion on the basis of the size, texture, surface gloss, and surrounding adhesion of the Achilles tendon. A 6-point scale was used to assess the severity of adhesion, applying the following criteria: 1. No adhesion (no postoperative adhesion); 2. Mild adhesion (rare adhesion); 3. Mild adhesion (localized adhesion); 4. Moderate adhesion (partial adhesion); 5. Severe adhesion (extensive adhesion); 6. Extremely severe adhesion (widespread adhesion). All the samples were independently scored by the six observers simultaneously, and the group allocation was blinded during the scoring process.

Biomechanical testing. At 8 weeks post-surgery, the rabbits were euthanized, and their Achilles tendons were harvested. The cross-section of the Achilles tendon was approximately elliptical. A Vernier calliper was used to measure the major and minor axes of the cross-section, and the cross-sectional area was calculated accordingly. A universal testing machine was used to apply a continuous tensile load at a constant rate of 20 mm/s until tendon rupture occurred. The ultimate tensile load and elongation at break were recorded. Young's modulus was calculated on the basis of the ultimate tensile load, cross-sectional area, and elongation at break ($n = 6$).

Statistical analysis

All the results were derived from at least three independent experiments. The data were analysed using ImageJ, Origin 2021, and GraphPad Prism 10.4.0. The data are presented as the mean ± standard deviation (SD). The sample size (n value) for each experiment is described in the 'Methods' section. Statistical significance was determined by one-way ANOVA, or multiway ANOVA. A p value < 0.05 was considered to indicate statistical significance (*$p < 0.05$, $p < 0.01$, *$p < 0.001$, ****$p < 0.0001$).

Reporting summary

Further information on research design is available in the Nature Portfolio Reporting Summary linked to this article.

Data availability

The Raw264.7 cell sequening data generated in this study have been deposited in the NCBI database under accession code PRJNA1371608. The other data generated in this study are provided in the Source Data file. Source data are provided with this paper.

References

1. Millar, N. L. et al. Tendinopathy. *Nat. Rev. Dis. Prim.* **7**, 1 (2021).
2. Hegedus, E. J. et al. Vascularity and tendon pathology in the rotator cuff: a review of literature and implications for rehabilitation and surgery. *Br. J. Sports Med.* **44**, 838–847 (2010).
3. Seow, D. et al. Lower re-rupture rates but higher complication rates following surgical versus conservative treatment of acute achilles tendon ruptures: a systematic review of overlapping meta-analyses. *Knee Surg. Sports Traumatol. Arthrosc.* **31**, 3528–3540 (2023).
4. Chan, J. J. et al. Epidemiology of Achilles tendon injuries in collegiate level athletes in the United States. *Int. Orthop.* **44**, 585–594 (2020).
5. Ochen, Y. et al. Operative treatment versus nonoperative treatment of Achilles tendon ruptures: systematic review and meta-analysis. *BMJ* https://doi.org/10.1136/bmj.k5120 (2019).
6. Huemer, M., Mairpady Shambat, S., Brugger, S. D. & Zinkernagel, A. S. Antibiotic resistance and persistence—implications for human health and treatment perspectives. *EMBO Rep.* **21**, e51034 (2020).
7. Bao, X. et al. Multifunctional biomimetic hydrogel dressing provides anti-infection treatment and improves immunotherapy by reprogramming the infection-related wound microenvironment. *J. Nanobiotechnol.* **22**, 80 (2024).
8. Shapouri-Moghaddam, A. et al. Macrophage plasticity, polarization, and function in health and disease. *J. Cell. Physiol.* **233**, 6425–6440 (2018).
9. Zhang, Q. et al. Chitosan/gelatin-tannic acid decorated porous tape suture with multifunctionality for tendon healing. *Carbohydr. Polym.* **268**, 118246 (2021).
10. Zhang, Q. et al. A biomimetic adhesive and robust Janus patch with anti-oxidative, anti-inflammatory, and anti-bacterial activities for tendon repair. *ACS Nano* **17**, 16798–16816 (2023).
11. Tang, Y. et al. Advances in preparation and application of antibacterial hydrogels. *J. Nanobiotechnol.* **21**, 300 (2023).
12. Chen, S. et al. Electrospun nanofibrous membranes meet antibacterial nanomaterials: from preparation strategies to biomedical applications. *Bioact. Mater.* **42**, 478–518 (2024).
13. Zhao, P. et al. Versatile hydrogel dressing with skin adaptiveness and mild photothermal antibacterial activity for methicillin-resistant Staphylococcus aureus-infected dynamic wound healing. *Adv. Sci.* **10**, 2206585 (2023).
14. Duan, Q., Tang, L., Xu, S., Yang, D. & Xu, Y. Metal ions-driven multienzyme activity of PEI-carbon dots-based nanozyme to improve antibacterial ability. *Chem. Eng. J.* **511**, 161957 (2025).
15. Quirós, J., Amaral, A. J. R., Pasparakis, G., Williams, G. R. & Rosal, R. Electrospun boronic acid-containing polymer membranes as fluorescent sensors for bacteria detection. *React. Funct. Polym.* **121**, 23–31 (2017).
16. Yao, K. et al. 3D printing of multiscale biomimetic scaffold for tendon regeneration. *Adv. Funct. Mater.* **35**, 2413970 (2025).
17. Kannus, P. Structure of the tendon connective tissue. *Scand. J. Med. Sci. Sports* **10**, 312–320 (2000).
18. Benjamin, M., Kaiser, E. & Milz, S. Structure-function relationships in tendons: a review. *J. Anat.* **212**, 211–228 (2008).
19. Zhong, D. et al. A strategy for tough and fatigue-resistant hydrogels via loose cross-linking and dense dehydration-induced entanglements. *Nat. Commun.* **15**, 5896 (2024).
20. Wang, Z. et al. A sprayable Janus hydrogel as an effective bioadhesive for gastrointestinal perforation repair. *Adv. Funct. Mater.* **34**, 2408479 (2024).
21. Xue, B. et al. Strong, tough, rapid-recovery, and fatigue-resistant hydrogels made of picot peptide fibres. *Nat. Commun.* **14**, 2583 (2023).
22. Yang, D. et al. Bacterial capture-killing capsules with remodeling bone immune microenvironment for the effective treatment of osteomyelitis. *Adv. Sci.* https://doi.org/10.1002/advs.202501505 (2025).
23. Xuan, W., Qu, Q., Zheng, B., Xiong, S. & Fan, G.-H. The chemotaxis of M1 and M2 macrophages is regulated by different chemokines. *J. Leukoc. Biol.* **97**, 61–69 (2015).
24. Cheng, Q. et al. Reprogramming exosomes as nanoscale controllers of cellular immunity. *J. Am. Chem. Soc.* **140**, 16413–16417 (2018).
25. Ala, M. The beneficial effects of mesenchymal stem cells and their exosomes on myocardial infarction and critical considerations for enhancing their efficacy. *Ageing Res. Rev.* **89**, 101980 (2023).
26. Shen, Y. et al. Sequential release of small extracellular vesicles from bilayered thiolated alginate/polyethylene glycol diacrylate hydrogels for scarless wound healing. *ACS Nano* **15**, 6352–6368 (2021).
27. Liu, L. et al. Endothelial cell-derived exosomes trigger a positive feedback loop in osteogenesis-angiogenesis coupling via upregulating zinc finger and BTB domain containing 16 in bone marrow mesenchymal stem cell. *J. Nanobiotechnol.* **22**, 721 (2024).
28. Dong, J., Wu, B. & Tian, W. Exosomes derived from hypoxia-preconditioned mesenchymal stem cells (hypoMSCs-exo): advantages in disease treatment. *Cell Tissue Res.* **392**, 621–629 (2023).
29. Cheng, P. et al. Hypoxia endothelial cells-derived exosomes facilitate diabetic wound healing through improving endothelial cell function and promoting M2 macrophages polarization. *Bioact. Mater.* **33**, 157–173 (2024).
30. Li, Q. et al. MiR146a-loaded engineered exosomes released from silk fibroin patch promote diabetic wound healing by targeting IRAK1. *Signal Transduct. Target. Ther.* **8**, 62 (2023).
31. He, Y. et al. Exosomes derived from tendon stem/progenitor cells enhance tendon-bone interface healing after rotator cuff repair in a rat model. *Bioact. Mater.* **40**, 484–502 (2024).
32. Zou, J. et al. Therapeutic potential and mechanisms of mesenchymal stem cell-derived exosomes as bioactive materials in tendon–bone healing. *J. Nanobiotechnol.* **21**, 14 (2023).
33. Cao, H., Duan, L., Zhang, Y., Cao, J. & Zhang, K. Current hydrogel advances in physicochemical and biological response-driven biomedical application diversity. *Signal Transduct. Target. Ther.* **6**, 426 (2021).
34. Peng, Z. et al. Dual-functionalized injectable pH-responsive hydrogels loaded with magnesium peroxide for the treatment of implant-associated infection. *ACS Appl. Mater. Interfaces* **16**, 68794–68815 (2024).
35. Chen, R. et al. HE@PCL/PCE Gel-nanofiber dressing with robust self-adhesion toward high wound-healing rate via microfluidic electrospinning technology. *ACS Appl. Mater. Interfaces* **15**, 46322–46332 (2023).
36. Lin, S. et al. Anti-fatigue-fracture hydrogels. *Sci. Adv.* **5**, eaau8528 (2019).
37. Dou, Y. et al. Endothelial cells-derived exosomes-based hydrogel improved tendinous repair via anti-inflammatory and tissue regeneration-promoting properties. *J. Nanobiotechnol.* **22**, 401 (2024).
38. Zheng, Z. et al. Self-growing hydrogel bioadhesives for chronic wound management. *Adv. Mater.* **36**, 2408538 (2024).
39. Ma, Y. et al. Bioinspired high-power-density strong contractile hydrogel by programmable elastic recoil. *Sci. Adv.* **6**, eabd2520 (2020).
40. Liang, Y., Li, Z., Huang, Y., Yu, R. & Guo, B. Dual-dynamic-bond cross-linked antibacterial adhesive hydrogel sealants with on-demand removability for post-wound-closure and infected wound healing. *ACS Nano* **15**, 7078–7093 (2021).
41. Han, X. et al. Exosome-coated oxygen nanobubble-laden hydrogel augments intracellular delivery of exosomes for enhanced wound healing. *Nat. Commun.* **15**, 3435 (2024).

42. Lv, Y. et al. Multi-crosslinked hydrogels with strong wet adhesion, self-healing, antibacterial property, reactive oxygen species scavenging activity, and on-demand removability for seawater-immersed wound healing. *Acta Biomater.* **159**, 95–110 (2023).
43. Cheng, S. et al. A motion-responsive injectable lubricative hydrogel for efficient Achilles tendon adhesion prevention. *Mater. Today Bio* **30**, 101458 (2025).
44. Yi, B. et al. Surface hydrophobization of hydrogels via interface dynamics-induced network reconfiguration. *Nat. Commun.* **15**, 239 (2024).
45. Wu, X. et al. An injectable asymmetric-adhesive hydrogel as a $GATA6^+$ cavity macrophage trap to prevent the formation of post-operative adhesions after minimally invasive surgery. *Adv. Funct. Mater.* **32**, 2110066 (2022).
46. Takai, Y., Ikeda, W., Ogita, H. & Rikitake, Y. The immunoglobulin-like cell adhesion molecule nectin and its associated protein afadin. *Annu. Rev. Cell Dev. Biol.* **24**, 309–342 (2008).
47. Patten, J. & Wang, K. Fibronectin in development and wound healing. *Adv. Drug Deliv. Rev.* **170**, 353–368 (2021).
48. Gałdyszyńska, M., Radwańska, P., Szymański, J. & Drobnik, J. The stiffness of cardiac fibroblast substrates exerts a regulatory influence on collagen metabolism via α2β1 integrin, FAK and src kinases. *Cells* **10**, 3506 (2021).
49. Zhang, Q. et al. Nanodot-inspired precise bacterial gene suppression in a smart hydrogel bandage for underwater wound healing. *Adv. Sci.* **12**, 2415169 (2025).
50. Costerton, J. W., Stewart, P. S. & Greenberg, E. P. Bacterial biofilms: a common cause of persistent infections. *Science* **284**, 1318–1322 (1999).
51. Zhang, S. et al. Tailoring versatile nanoheterojunction-incorporated hydrogel dressing for wound bacterial biofilm infection theranostics. *ACS Nano* **19**, 10922–10942 (2025).
52. Krawczenko, A. & Klimczak, A. Adipose tissue-derived mesenchymal stem/stromal cells and their contribution to angiogenic processes in tissue regeneration. *Int. J. Mol. Sci.* **23**, 2425 (2022).
53. Kalluri, R. & LeBleu, V. S. The biology, function, and biomedical applications of exosomes. *Science* **367**, eaau6977 (2020).
54. Wang, Y. et al. Adipose mesenchymal stem cell derived exosomes promote keratinocytes and fibroblasts embedded in collagen/platelet-rich plasma scaffold and accelerate wound healing. *Adv. Mater.* **35**, 2303642 (2023).
55. Li, D. Restoring tendon microenvironment in tendinopathy: macrophage modulation and tendon regeneration with injectable tendon hydrogel and tendon-derived stem cells exosomes. *Bioact. Mater.* **47**, 152–169 (2025).
56. Bai, X. et al. Macrophage polarization in cancer and beyond: from inflammatory signaling pathways to potential therapeutic strategies. *Cancer Lett.* **625**, 217772 (2025).
57. Liu, X. et al. Nonswellable hydrogel patch with tissue-mimetic mechanical characteristics remodeling In vivo microenvironment for effective adhesion prevention. *ACS Nano* **18**, 17651–17671 (2024).
58. Usuda, K. et al. Expression and prognostic impact of VEGF, CD31 and αSMA in resected primary lung cancers. *Anticancer Res.* **38**, 4057–4063 (2018).
59. Mascharak, S. et al. Multi-omic analysis reveals divergent molecular events in scarring and regenerative wound healing. *Cell Stem Cell* **29**, 315–327.e6 (2022).
60. Mascharak, S. et al. Preventing *engrailed-1* activation in fibroblasts yields wound regeneration without scarring. *Science* **372**, eaba2374 (2021).
61. Li, Y. et al. Integrating electrospun aligned fiber scaffolds with bovine serum albumin-basic fibroblast growth factor nanoparticles to promote tendon regeneration. *J. Nanobiotechnol.* **22**, 799 (2024).
62. Wang, X. et al. Mussel-derived bioadaptive artificial tendon facilitates the cell proliferation and tenogenesis to promote tendon functional reconstruction. *Adv. Healthc. Mater.* **12**, 2203400 (2023).
63. Liu, S. et al. Tendon healing and anti-adhesion properties of electrospun fibrous membranes containing bFGF loaded nanoparticles. *Biomaterials* **34**, 4690–4701 (2013).
64. Pang, S. et al. Use of a pH-responsive imatinib mesylate sustained-release hydrogel for the treatment of tendon adhesion by inhibiting PDGFRβ/CLDN1 pathway. *Bioact. Mater.* **38**, 124–136 (2024).
65. Jiang, Y., Zhu, C., Ma, X. & Fan, D. Tough and anisotropic janus hydrogel for tendon injury repair with controlled release of bFGF in tendon microenvironment. *Chem. Eng. J.* **500**, 157139 (2024).
66. Li, H. et al. Strong and fatigue-resistant hydrogels via poor solvent evaporation assisted hot-stretching for tendon repair. *Adv. Sci.* https://doi.org/10.1002/advs.202503697 (2025).
67. Pranantyo, D. et al. Hydrogel dressings with intrinsic antibiofilm and antioxidative dual functionalities accelerate infected diabetic wound healing. *Nat. Commun.* **15**, 954 (2024).
68. Rogers, C., Tseng, D. Y., Squire, J. C. & Edelman, E. R. Balloon-artery interactions during stent placement: a finite element analysis approach to pressure, compliance, and stent design as contributors to vascular injury. *Circ. Res.* **84**, 378–383 (1999).
69. Santander-Borrego, M. et al. Hydrogels with lotus leaf topography: investigating surface properties and cell adhesion. *Langmuir* **33**, 485–493 (2017).
70. Wilson, D. N. Ribosome-targeting antibiotics and mechanisms of bacterial resistance. *Nat. Rev. Microbiol.* **12**, 35–48 (2014).
71. Wang, Y., Tu, S., Pinchuk, A. N. & Xiong, M. P. Active drug encapsulation and release kinetics from hydrogel-in-liposome nanoparticles. *J. Colloid Interface Sci.* **406**, 247–255 (2013).
72. Zhang, X. et al. Essential roles of exosome and circRNA_101093 on ferroptosis desensitization in lung adenocarcinoma. *Cancer Commun.* **42**, 287–313 (2022).

Acknowledgements

This work was supported by the Natural Science Foundation of Shanghai (Grant No. 24ZR1480700, Shuo F). The manuscript has been professionally edited by American Journal Experts (AJE) for English language polishing, including grammar refinement, academic expression optimization, and journal formatting adjustments. The editing process adhered strictly to COPE ethical guidelines without altering the research data or conclusions. Certification details are available via the AJE validation system (ID: E896-E30F-2655-4CDB-6D0P).

Author contributions

Jie Li designed the research protocol, performed core experimental operations, collected and organized experimental data, and participated in drafting and revising the manuscript; Zishuo Wang assisted in core experiments, conducted statistical analysis of partial data, and participated in figure preparation and result validation; Wenjing Yang participated in sample preparation and detection experiments, sorted raw data, and assisted in writing the methodology section of the manuscript; these three authors contributed equally to this work. Yuchen Zhang conducted literature research and review, participated in the optimization of experimental design, and assisted in data analysis and discussion; Yanjun Wang performed auxiliary experimental operations, collected partial clinical/sample data, and participated in the preparation and management of experimental materials; Xuhui Wang assisted in experimental data validation, was responsible for the configuration and quality control of partial experimental reagents, and participated in preliminary result analysis; Hongrui Wang participated in sample processing and detection, organized experimental records, and assisted in compiling supplementary materials of the manuscript; Yang Xie conducted in vitro experimental validation, was responsible for data entry and preliminary screening, and assisted in figure optimization; Shuogui

Xu provided technical support for core experiments, participated in quality control during experiments, and organized experimental related documents; Yan Shang provided clinical sample resource support, participated in the verification and organization of clinical data, and assisted in writing the discussion section. Chunyu Xue (Co-corresponding Author)* guided research design, coordinated experimental directions, verified the authenticity and completeness of experimental data, and led the revision and finalization of the manuscript; Yuntong Zhang (Co-corresponding Author)* guided data analysis strategies, participated in the demonstration of core conclusions, coordinated cooperation among authors, and provided experimental platform support; Shuo Fang (Corresponding Author)* proposed the research concept, designed the overall technical route, guided experimental implementation and data interpretation, provided research funding support, and was responsible for the final review and submission of the manuscript.

Competing interests

The authors declare no competing interests.

Additional information

Supplementary information The online version contains supplementary material available at https://doi.org/10.1038/s41467-026-68514-0.

Correspondence and requests for materials should be addressed to Chunyu Xue, Yuntong Zhang or Shuo Fang.

Peer review information *Nature Communications* thanks Xianai Shi, Yi Wang, and the other, anonymous, reviewer(s) for their contribution to the peer review of this work. A peer review file is available.